Charles University in Prague
Faculty of Mathematics and Physics

DIPLOMA THESIS

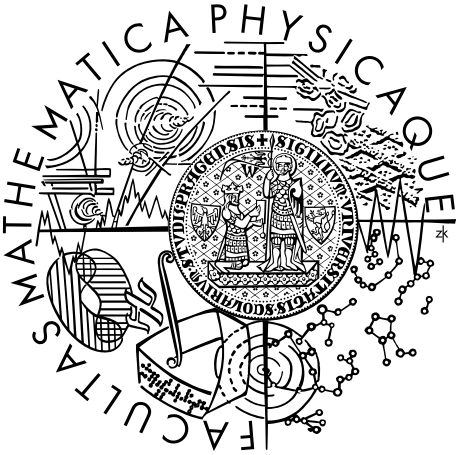

Zbyněk Drásal

Simulation of Charge Collection in Semiconductor Microstrip Detectors

Institute of Particle and Nuclear Physics

Supervisor: Dr. Zdeněk Doležal
Co-Supervisor: Dr. Peter Kodyš

Study programme: Nuclear and Subnuclear Physics

Tato práce je věnována Balimu.
This work is dedicated to Bali.

Velice rád bych využil této příležitosti a poděkoval všem, kteří mě uvedli do problematiky detekce vysokoenergetických částic pomocí křemíkových stripových detektorů, umožnili mi se zapojit do testování těchto zařízení v Praze a výrazně mi pomohli při vytváření simulačního softwaru.

Obzvláště jsem velmi vděčný za celkově profesionální přístup ze strany svého školitele Dr. Zdeňka Doležala, za jeho velmi cenné rady a inspirativní diskuse. Zároveň mu děkuji za zprostředkování kontaktu s Dr. Nicolou Mazziottou a Dr. Francescem Loparcem z INFN-Sezione di Bari, od nichž jsem měl možnost získat nejen spoustu hodnotných rad týkajících se simulace sběru náboje v stripovém detektoru, ale i fortranovský program simulace propagace elektron-děrových párů v křemíku. Za což jim oběma patří zvláštní díky.

V neposlední řadě chci poděkovat Dr. Petru Kodyšovi za rady a pomoc, kterou mi poskytnul při odladění simulace odezvy detektoru na laserový signál, za poskytnutí naměřených dat a za detailní vysvětlení problematiky laserového testování. A nakonec bych chtěl poděkovat za pomoc a velmi přátelské rady ze strany Mgr. Pavla Řezníčka. Hodně mi pomohl nejen v oblasti programovacích technik, které se používají ve fyzice vysokých energií, a v oblasti správy operačního systému Unix, ale i s řešením zdánlivě triviálních problémů nejen z oblasti fyziky.

Prohlašuji, že jsem svou diplomovou práci napsal samostatně a výhradně s použitím citovaných pramenů. Souhlasím se zapůjčováním práce.

V Praze dne 21.dubna 2006

On the occasion, I would like to thank all the people who have introduced me into the problematics of high energy particle detector systems – silicon microstrip detectors, who have let me participate in testing of SCT modules in Prague and who extremely have helped me with creating the simulation software.

Particularly, I'm very grateful to my supervisor Dr. Zdeněk Doležal for his completely professional approach, for valuable advice and very inspiring discussions. Simultaneously, I would like to thank him for making contact with Dr. Nicola Mazziotta and Dr. Francesco Loparco from INFN-Sezione di Bari, who have provided me not only with a lot of helpful information, that concern the simulation of charge collection in microstrip detectors, but also with the FORTRAN code of charge collection process simulation. My special thanks belong to both of them.

Last but not least, I want to thank Dr. Peter Kodyš for advice and help, he offered me during debugging process of the simulation of detector response to the laser signal. I also want to thank him for providing me with measured laser data and for very detailed description, how the laser testing system is functioning. Finally, I'd like to express a lot of thanks to Mgr. Pavel Řezníček. Not only for very friendly advice and help with Unix system administration and with various techniques of programming, used in high energy physics, but also with finding solution to at first sight trivially looking problems concerning not only physics.

I declare, that I wrote my diploma thesis independently and exclusively with the use of cited sources. I approve of lending the thesis.

Prague, April 21, 2006

Contents

Název práce: *Simulace sběru náboje v křemíkových stripových detektorech*

Autor: *Zbyněk Drásal*

Katedra: *Ústav částicové a jaderné fyziky*

Vedoucí diplomové práce: *RNDr. Zdeněk Doležal, Dr., ÚČJF*

E-mail vedoucího: *Zdenek.Dolezal@mff.cuni.cz*

Abstrakt: Předložená diplomová práce se zabývá detailním studiem sběru náboje v křemíkových stripových detektorech (SCT) navržených pro vnitřní detekční systém detektoru ATLAS. Za tímto účelem byla vyvinuta dvou-dimenzionální simulace sběru náboje metodou Monte Carlo a byla implementována do softwarového prostředí Geantu 3. K ověření její správnosti byla využita experimentální data naměřená v letech 1999–2004 na testovacích svazcích v CERNU.

Vlastní simulace je navržena takovým způsobem, aby bylo možné studovat odezvu detektoru jak na ionizující částici, tak i na laserový svazek gausovského profilu a definované vlnové délky. Konkrétně se práce zabývá studiem vlivu jednotlivých fyzikálních procesů (efekt sdílení náboje, difuze, δ-elektrony, atd.) na vytváření a šíření elektron-děrových párů v křemíkovém detektoru, srovnáním výsledné simulace s daty z test. svazků a vlastní interpretací experimentálních výsledků.

Dále byly na základě srovnáni simulace s měřeními získanými z laseru (1060 nm) objeveneny specifické efekty související s vytvářením elektron-děrových párů laserovým svazkem. Tyto efekty bylo možno vysvětlit na základě srovnání simulace s novým měřením.

Klíčová slova: *Monte Carlo, simulace, Geant 3, křemíkový stripový detektor, SCT ATLAS, testy na svazku, laser testy*

Title: *Simulation of Charge Collection in Semiconductor Microstrip Detectors*

Author: *Zbyněk Drásal*

Department: *Institute of Particle and Nuclear Physics*

Supervisor: *Dr. Zdeněk Doležal, IPNP*

Supervisor's e-mail address: *Zdenek.Dolezal@mff.cuni.cz*

Abstract: This diploma thesis deals with the detailed study of charge collection in silicon microstrip detectors (SCT) designed for the Inner Tracker of ATLAS detector system. For this purpose a two dimensional Monte Carlo simulation implemented in Geant 3 framework has been developed and the software validity on beam tests data measured in CERN in 1999-2004 has been verified.

The simulation allows to study the response of a silicon detector to both an ionizing elementary particle and a laser beam of gaussian profile and a certain wavelength. In our case the influence of individual physical processes (charge sharing effect, diffusion, δ-rays, etc.) leading to the generation and propagation of e-h pairs in a silicon material has been examined and based on the comparison of the simulations with the real beam tests data the obtained results have been interpreted.

The Monte Carlo simulation has been also performed for the laser (1060 nm) tests and a few effects specific for e-h pairs generation by a laser beam have been found. In order to explain them a new laser scan has been made and with the help of simulation interpreted.

Keywords: *Monte Carlo, Simulation, Geant 3, Silicon microstrip detector, SCT ATLAS, Beam tests, Laser tests*

Introduction

In the last ten years semiconductor devices have experienced a rapid development in a large variety of fields in science and technology, including nuclear physics, x-ray astronomy and elementary particle physics. All these developments have grown out of the need for new investigative tools for basic research. The success of (silicon) semiconductor devices is due to several unique properties that are not available with other types of detectors. Let us introduce a few of them: the combination of precise position measurements (in order of a few μm) with high readout speed, simultaneous measurement of momentum and position when placed in a magnetic field and finally, the possibility of integrating detector and its readout electronics on the same substrate.

In the CERN (the European Organization for Nuclear Research) a new hadron collider LHC (Large Hadron Collider) is being built. For this purpose four large experiments are being prepared, one of them is the detector system ATLAS (A Toroidal LHC ApparatuS). The semiconductor microstrip detectors, usually called the SemiConductor Trackers (SCT), form one important part of the ATLAS Inner Detector System. The main function of SCT is to precisely measure the momentum and the vertex position of charged particles produced in a proton-proton collision.

A lot of interest and effort of many physicists and other people involved in ATLAS collaboration have concentrated on development and testing of individual subsystems and components of ATLAS detector system. One of the groups that have participated in the project and have focused on Inner Detector System, namely on semiconductor microstrip detectors, is the group of VdG accelerator at Institute of Particle and Nuclear Physics at Charles University in Prague. Parallel to these activities the VdG group developed two specially designed testing methods of semiconductor devices: the method using β^- radioactive source and the method using infrared laser beam.

For comparison of experimental results obtained by various methods it is very useful to develop a two dimensional Monte Carlo simulation, simulating charge generation processes and charge collection process. For this purpose the main aim of this diploma thesis was: to develop such a simulation, implement it in Geant 3 framework, verify its corectness on real beam test data,

explain how particular physical effects influence the experimental results and finally, to simulate the detector response to the laser signal and extract from the comparison of simulated data and measured data the characteristics of laser beam and the properties of detector. Moreover, based on the simulation, it is very desirable to suggest new possible interesting measurements.

In the first chapter of the thesis the focus is given on a brief introduction to the whole ATLAS detector, its SCT subsystem and on detailed description of SCT module construction and read-out system. Physical properties of silicon microstrip detectors as well as features that concern interactions of a particle in a silicon material and absorption of light in a silicon material are reviewed in chapter 2. Chapter 3 is devoted to the detailed description of simulation conception, its implementation in Geant 3 framework and to explanation of Monte Carlo results. In chapter 4, the simulation is verified on real beam test data, measured in CERN in 1999–2004, and an analysis of simulation results in comparison with experimental results is made. The last chapter, chapter 5, is dedicated to the laser simulation. Here, briefly the laser method is described, the experimental results are presented and finally, the analysis of simulation results together with measurements is done.

1 Detector ATLAS

1.1 Purpose of ATLAS System

The ATLAS detector (A Toroidal LHC Apparatus) [2] is a general purpose p-p detector system and is designed to exploit the full discovery potential of the Large Hadron Collider (LHC). The collider is now being built at CERN, the world's largest international laboratory of nuclear and subnuclear research. It is placed near Geneve in Switzerland, at the border with France, but numerous facilities and buildings, including the most of the collider and also the Super Proton Synchrotron (SPS) beam test beamlines, are situated in France. The LHC, see fig. 1.1, is a proton-proton collider with designed

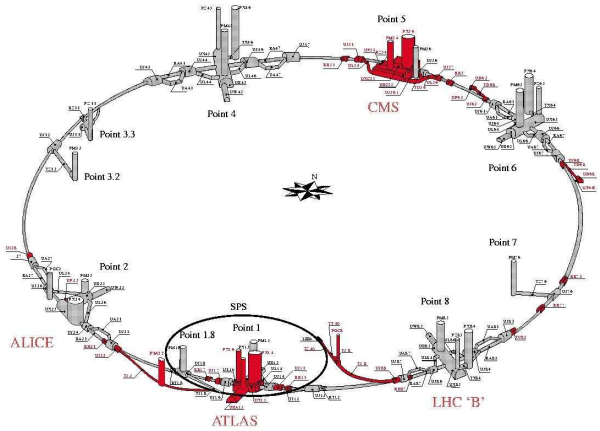

Fig. 1.1: The Large Hadron Collider

luminosity of $10^{34}\,\mathrm{cm}^{-2}\mathrm{s}^{-1}$ and expected energy of interacting hadrons 7 TeV. The beam bunch-crossing frequency will reach 40 MHz and at the highest luminosity about 20 interactions are expected. Due to these extreme features LHC offers a large range of physics opportunities.

The major interest is the quest for the origin of the different particle masses at the electroweak scale. The physical effect of mass generation is based on the so-called spontaneous symmetry breaking mechanism of the Standard Model (SM). One of the possible manifestation of the spon-

taneous symmetry breakdown could be the existence of a SM Higgs boson or of a family of Higgs particles when considering Minimal Supersymmetric extension of SM (MSSM). Because cross sections of physics lying behind these extensions are very small, the ATLAS detector has to be sensitive to various processes involving either a Higgs boson or the whole MSSM Higgs family.

Other important goals are the search for heavy W-like and Z-like objects and for supersymmetric particles. Besides that, an effort will be made to find an evidence of compositeness of the quarks as well as the leptons, to investigate the CP violation in B-decays and to study top quark physics in detail. Emphasis will also be put into the performance necessary for the physics visible during the initial lower intensity running ($10^{33}\,\mathrm{cm}^{-2}\mathrm{s}^{-1}$).

The set of ATLAS physics aims makes a lot of demands on the basic design criteria: very good electromagnetic calorimetry for electron and photon identification and measurement; efficient tracking at high luminosities for lepton momentum measurements, for b-quark tagging and for enhanced electron and photon identification as well as τ lepton and heavy flavour vertexing and reconstruction at lower luminosity; stand-alone, high precision momentum measurements; large acceptance in η[1] coverage and finally, triggering and measurements of particles at low-p_T thresholds.

1.2 Design and Construction

The overall detector layout can be seen in figure 1.2. Total length of the detector is about 44 m and height about 22 m. Its dimensions are comparable to a five floor building and approximate weight will reach 7000 tons.

The magnet configuration is formed by an inner detector superconducting solenoid of 2 T around the inner detector cavity and large superconducting air-core toroids consisting of independent coils outside the calorimetry. The total magnet system will represent a cold mass of 700 tons and a total weight of 1400 tons.

The part nearest to the interaction point is called the Inner Detector (see fig. 1.3). It is located inside a cylinder of length 6.80 m and radius 1.15 m. The main goal of the system is to precisely measure momentum, particle tracks and with high accuracy to determine interaction vertices. All this can be achieved with a combination of discrete high-resolution pixel and strip detectors in the inner part and continuous straw-tube tracking detectors with transition radiation capability in the outer part. Mechanically, the Inner Detector consists of three units: a barrel part extending over ±80 cm and

[1]Pseudorapidity η is defined by the formula: $\eta = -\ln\tan(\frac{\vartheta}{2})$

two identical end-caps covering the rest of the cylindrical cavity. In the barrel, the high precision detector layers are arranged on concentric cylinders

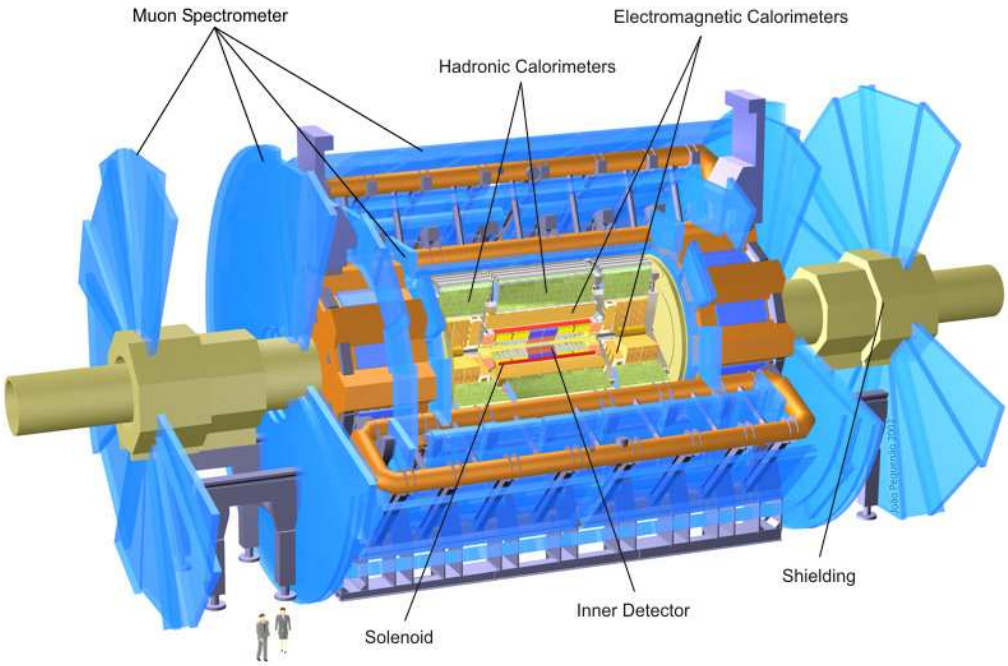

Fig. 1.2: ATLAS Detector Layout

around beam axis in the region with $|\eta| < 1$, while in the end-caps detectors are mounted on discs perpendicular to the beam axis. The overall pseudorapidity coverage is $|\eta| < 2.5$. The pixel system, 140 million detector elements, each $50\,\mu$m in the $R\Phi$ direction and $300\,\mu$m in z-direction, provides at least three precision measurements over all the acceptance. The SCT system, $61\,\mathrm{m}^2$ of silicon detectors with 6.2 million readout channels and divided to 4 barrel layers and 2 sets of 9 end-cap discs, is designed to provide at least four precision measurements per track in the intermediate radial range. Finally, the Transition Radiation Tracker (TRT), based on the use of straw detectors, each 4 mm in diameter and filled with xenon gas for better capability of transition radiation photons detection, contributes to the accuracy of the momentum measurement with providing approximately 36 hits per track. More details can be found in [3] and [4].

Around the Inner Detector there is a higly granular Liquid Argon (LAr) eloctromagnetic sampling calorimetry with excellent performance in terms

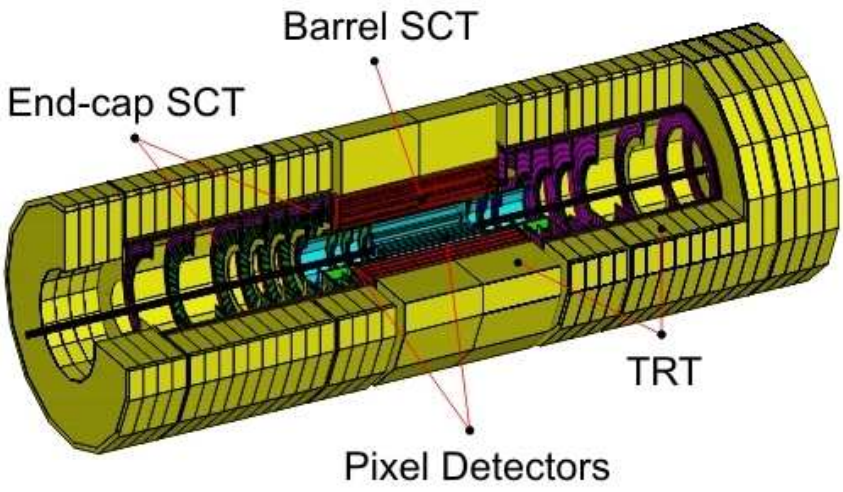

Fig. 1.3: Inner Detector Layout

of energy and positions resolutions. The same technology is also used for hadronic calorimetry in the end-caps and for special LAr forward calorimeters with extended η coverage (from $|\eta| < 3.2$ to $|\eta| < 4.9$). All LAr calorimeters are put into the cryostats to ensure sufficiently low temperature. In the barrel region, the hadronic calorimetry uses iron absorbers with scintillator plates. This technology is based on a sampling technique with plastic scintillator tiles placed in planes perpendicular to the beam axis, embedded in an iron absorber and read out by wavelength shifting fibres. The LAr calorimetry is contained in a cylinder with an outer radius of 2.25 m and $\pm$6.65 m along the beam axis. The outer radius of the tile calorimeter is 4.25 m and its length is $\pm$6.10 m. The supposed weight is about 4000 tons.

The calorimeter is surrounded by the muon detector system that involves three layers of chambers in the barrel part and three or four layers in the end-cap part. In the barrel, the layers of chambers are placed at the inner and outer edges of the magnetic volume. In the forward direction the chambers are placed at the front and back faces of the cryostats, with a third layer against the cavern wall. In design a new chamber concept of the Monitored Drift Tubes (MDTs) have been implemented and the chambers will be used over a very large part of the η acceptance. The older concept, the Cathode Strip Chambers (CSCs), are used in the region of large rapidity. The muon system is complemented with an independent fast trigger chamber system

with two different technologies being used: Resistive Plate Chambers (RPC) in the barrel part and Thin Gap Chambers (TGC) in the forward regions. The RPC is a gaseous parallel plate detector with a few ns time resolution. The TGC is a wire chamber operating in saturated mode. The basic measurement in each muon chamber is a track segment, providing a vector for robust pattern recognition and momentum determination. The muon spectrometer defines the overall dimensions of the ATLAS detector system. The outer chambers of the barrel are at a radius of about 11 m. The length of the barrel toroid coils is ±13 m and the third layer of the forward muon chambers, mounted on the cavern wall, is located at ±21 m from the interaction point.

The ATLAS trigger system is organized in three trigger levels (LVL1, LVL2, LVL3) in the following way. At LVL1, special-purpose processors act on reduced-granularity data from a subset of the detectors. The LVL2 trigger uses full-granularity, full-precision data from most of the detectors and examines only regions of the detectors identified by LVL1. Only these regions contain interesting information. At LVL3, the full event data are used to make final selection of events to be recorded for offline analysis. The LVL1 reduces full LHC bunch-crossing rate of 40 MHz to the maximal frequency of 100 kHz. The LVL2 trigger lowers then the frequency from up to 100 kHz to about 1 kHz. Such a massive reduction of frequency is necessary due to incredibly large amount of data collected from the whole ATLAS.

1.3 SCT Modules

The Semiconductor Tracker System is based upon silicon microstrip technology and consists of three individual parts: a barrel and two end-caps. The barrel part is formed from four layers arranged on concentric cylinders around the beam axis and placed in the central part. The end-caps are mounted on nine discs, symmetrically to the interaction point and perpendicularly to the beam axis. The overall layout of SCT is depicted in fig. 1.4.

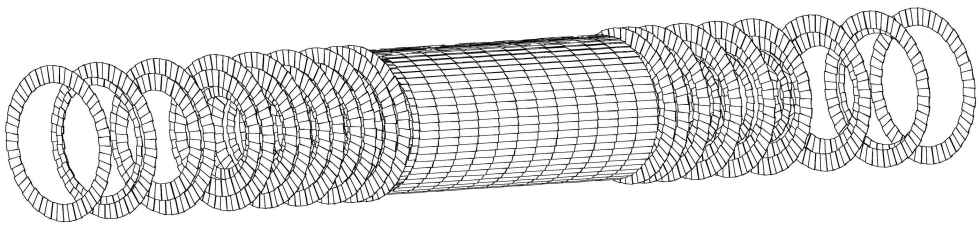

Fig. 1.4: SCT Layout

1.3.1 Module Description

The basic sub-unit of the tracker is a module. Due to different position and geometry of individual parts of the tracker, one can divide the modules into two basic categories: barrel modules and end-cap modules (see fig. 1.5). Moreover, end-cap modules can be found in four variants: Inner Module,

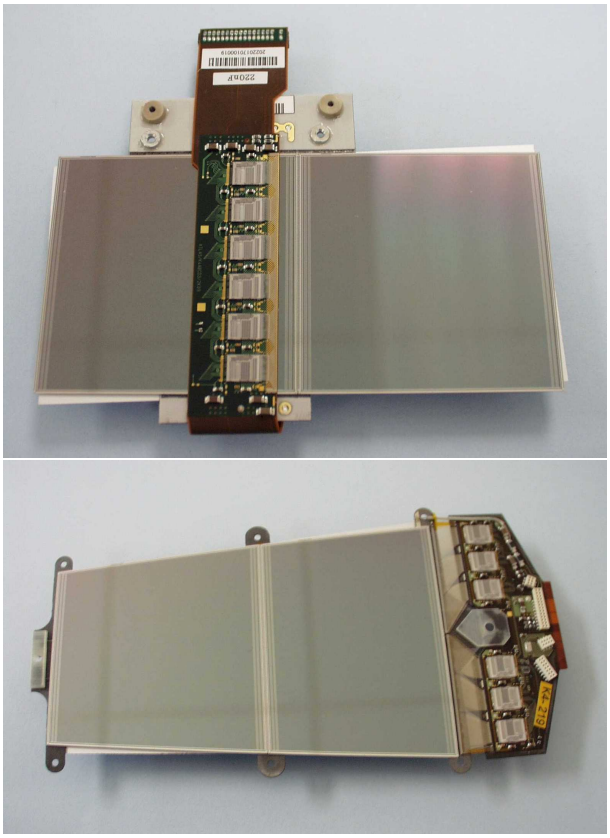

Fig. 1.5: The Barrel Module (top) and the End-Cap Module (down)

Short Middle Module, Middle Module and Outer Module.

In the barrel region, each module is made of four 6.4 cm × 6.36 cm single sided silicon microstrip wafers. The wafers are wire bonded (electrically connected) to each other to provide effectively one sensitive detector plane 12 cm long. In order to form a double sided detector, these two mechanical units are glued back-to-back with a stereo angle of 40 mrad to each other, with a mechanical basement – spine inside, and connected via a glass fan-in to the hybrid with 12 specially designed ABCD chips. The spine serves as a mechanical support for the wafers and increases the thermal conductivity in the plane of the module. The fan-in forms a connection between sensors

and a hybrid and acts as a thermal break to prevent heat from the front-end electronics from entering into the silicon wafers. All the wafers are single sided 285 μm thick p-in-n detectors, that form a p-n junction. There are $768 + 2$ Al strips on each wafer, but only 768 strips are active. The first strip and the last one are being used for electric field shaping. For the p^+ implants and the strips two different technologies from two detector producers: Hamamatsu[2] and CiS[3], have been used. The first technology is mainly used for barrel and end-cap modules, the latter for end-cap modules. Both of them are shown in fig. 1.6. The strip pitch, the distance between 2 strips, is designed constant – 80 μm. As far as the measurement precision is concerned, one side of the detector measures the $R\Phi$ coordinates (axial strips) while the other

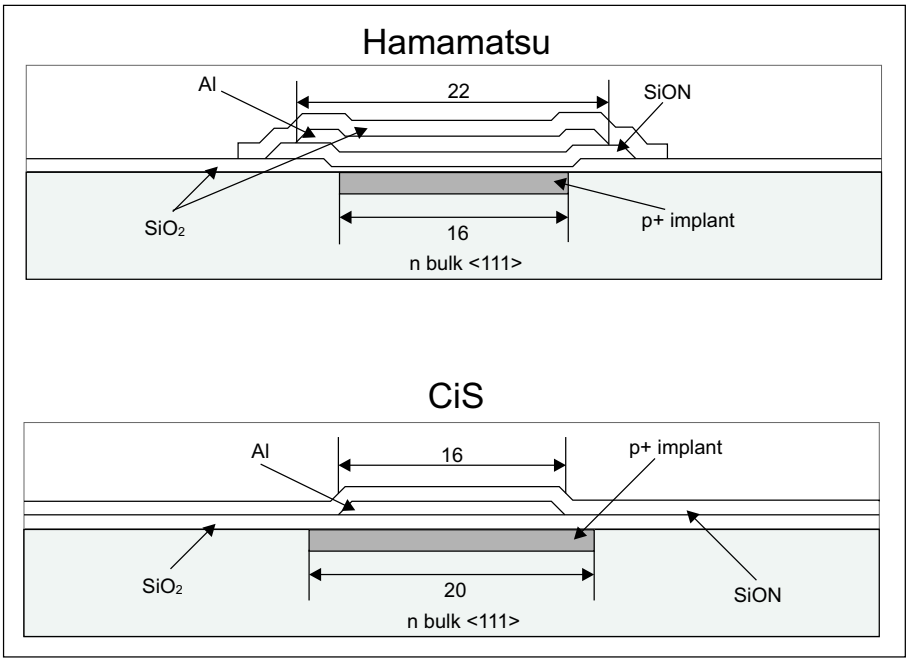

Fig. 1.6: Two Different Technologies of Strip Design

side measures the 40 mrad rotated coordinates. Combination of two points from both detector planes gives the resolution: 16 μm in the $R\Phi$-direction and 580 μm in z-direction.

In the end-cap region, the modules differ from the barrel ones in the following ways. The wafers are wedge-shaped, so the strips are not parallel and converge to one point close to the beam line for easy extraction of Φ coordinate of the track. Further, the strip pitch is not constant: for the Inner

[2]Hamamatsu Photonics, `www.hamamatsu.com`
[3]CiS Institut fűr Mikrosensorik, `www.cismst.de`

Detector it varies from 54.4 μm to 69.5 μm, for the Middle from 70.3 μm to 94.8 μm and for the Outer from 70.8 μm to 90.3 μm. Finally, the module planes are perpendicular to the beam axis, so the last mentioned precision is not in z-direction, but in R-direction. The overall picture of end-cap module is shown in fig 1.7.

Read-out of the detector is provided by the front end read-out electronics. To ensure low noise operation, the front end electronics (FE) is assembled immediately at the strips electrode into a hybrid. There are 12 ABCD

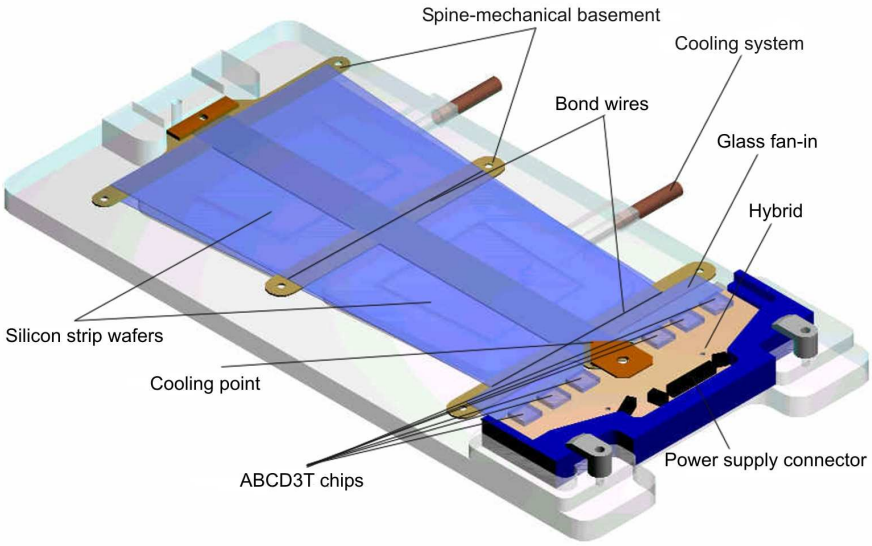

Fig. 1.7: Module Description

chips there, each reading 128 channels. In order to reduce the amount of taken data, the SCT uses binary read-out system. The signal is compared to the given threshold and a binary result of the comparison (0×1) is sent for each strip to the pipeline and waits for further processing. The information is held there for the duration of the LVL1 trigger and waits for the decision whether the binary result will be transmitted or discarded. If the data are to be sent further, they are compressed and transmitted out using optical fibers. The schematic picture of the FE can be seen in fig. 1.8. Very important for the electronics is the calibration circuit. It enables to associate the threshold on the discriminator to an appropriate charge at the input of the amplifier. To obtain the best possible uniformity of the calibration process, threshold can be adjusted individually channel by channel. This process is called trimming. Another advantageous feature is a possibility to

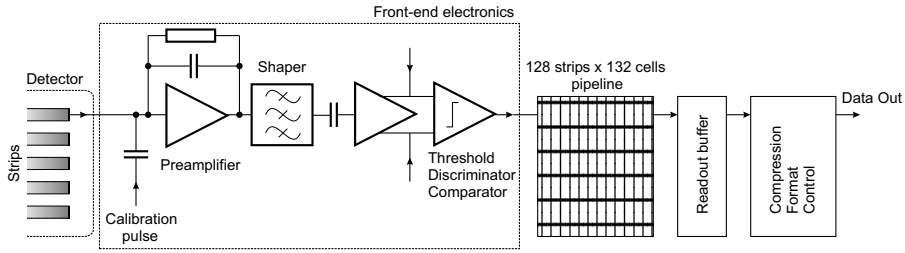

Fig. 1.8: Front End Electronics Scheme

bypass a non-functional chip or to use a redundant optical fibre to fix possible failure.

1.3.2 Laboratory Module Read-out System

The schematic figure 1.9 of a basic module controller and a read-out system, based on Versa Module Eurocard (VME) technology, is used from [18] for an explanation of how the whole system is functioning:

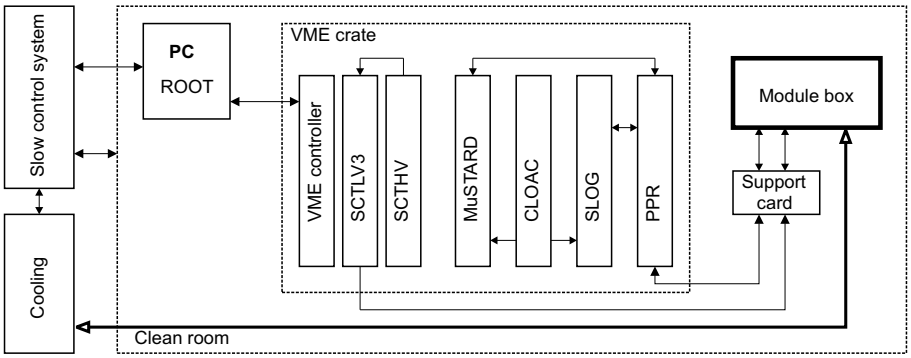

Fig. 1.9: Module Controller and Read-out System

- VME CONTROLLER – assures communication between the module and a personal computer.
- SCTLV3 MODULE – provides low digital voltage (4 V), analog voltage (3.5 V) and other control voltages for the module read-out electronics and assures monitoring of temperature and power consumption.
- SCTHV MODULE – provides bias voltage for the detector and monitors the leakage current.

- MuSTARD MODULE – reads out and stores the data sent from a hybrid.
- CLOAC and SLOG MODULES – generate command sequences like trigger, calibration and reset signals. The reset signals are sent to the chips to reconfigure them and correct possible loss of a threshold or other settings information. The CLOAC card has another advantage: it enables to use an external trigger system.
- PPR – with the support card are passive components connecting data links from the hybrid and the VME.

The data acquisition software (SCTDAQ) is based on a C++ interpreter ROOT [25] with special classes for easy data manipulation and visualisation. The software contains a control panel, an interactive window and a basic information panel showing DCS, the data control monitoring system. More information about the system and testing set-up can be found on the web pages [19].

2 Silicon Detectors

In this chapter, the basics of detector physics [14] as well as silicon semiconductor physics [21] will be summarized. The focus will be particularly given on the semiconductor structure that the silicon microstrip detector is based on, the p-n junction, and on the interactions of particles and light in silicon devices. At last the detailed description of properties of silicon microstrip detector will be made.

2.1 Advantages and Disadvantages

Compared with other materials, silicon has unique physical properties that makes it suitable for use in high energy physics. The most important features of silicon, resp. silicon detectors, are summarized here:

- A small value of average energy 3.65 eV needed for creation of one electron-hole pair leads to a large number of charge carriers created per unit length of silicon material by an ionizing particle. Such a small energy of 3.65 eV is related to the value of silicon band gap (1.12 eV). If we take for example MIP[1] traversing 285 μm thick silicon bulk, we will get around 24 500 e-h pairs. In comparison with gaseous detectors, the ionizing energy is an order of magnitude higher and the number of created carriers will be substantially lower.

- High density of silicon material (2.33 g/cm^3) causes that a particle traversing the detector loses approximately more energy per unit length than for instance in gaseous detectors. Moreover, it is possible to build thin detectors that hold still large enough signal to be measured, but minimize the number of δ-electrons and multiple scattering. Typical thickness of SCT detectors is 285 μm.

- Even though the mobility of electrons (1450 cm^{2}V^{-1}s) and holes (450 cm^{2}V^{-1}s) at room temperature is influenced by doping, the dependence

[1] A minimum ionizing particle, e.g. 180 GeV/c pion

is very moderate in large range of concentrations and carriers can move almost as free particles. This effect results in rapid collection of charge carriers (∼10 ns) and thus the detectors can be used in high-rate environment.

- The silicon wafers are mechanically rigid, no additional supporting structure is needed.
- Read-out and front end electronics is based on the same silicon technology and can be integrated into a single device.

Besides that, the silicon detectors have also disadvantages. Very crucial is their high cost and possible radiation damage in high radiation environment as for instance LHC forms.

2.2 Basic Silicon Properties

Silicon, an element of IV group (Z = 14, A = 28.086), crystallizes in a diamond lattice structure (lattice constant = 5.43 Å). Its basic properties can be described in a band model, where electron energies are constrained to lie in bands. The last completely filled band at zero temperature is called a valence band and the first empty band is called a conduction band. The two bands are separated from each other by the band gap, an area where no energy levels exist. At higher temperatures the thermal vibrations can break the covalent bonds of individual atoms and a fraction of the electrons from the valence band is excited to the conduction band. The empty states, holes, left behind the excitation and created in the valence band behave under electric field as positive particles. Therefore, both the electrons and the holes contribute together to the total electric current. The semiconductor that contains a relatively small amount of impurities is called intrinsic.

Intrinsic semiconductors are rarely used in semiconductor devices since it's extremely hard to obtain sufficient purity in the material. Moreover, in most cases, one intends to change semiconductor properties. By replacing a small fraction of silicon atoms with another type with higher (V group, e.g. phosphorus) or lower (III group, e.g. boron) number of valence electrons, one can obtain n-type, resp. p-type, semiconductors. In first case we say that the electron is "donated" to the conduction band and the foreign atom is called donor. In the latter case we say that the electron is "accepted" to form four covalent bonds around the foreign atom, acceptor, and a hole is created in the valence band. During the procedure, called impurities doping, the semiconductor becomes extrinsic with new energy levels introduced in

band gap and one concentration of carriers dominant (majority carriers) and the other one negligible (minority carriers). For intrinsic semiconductors both concentrations are the same, but at room temperature substantially lower.

In thermal equilibrium the intrinsic electron concentration in conduction band can be evaluated from the following relation:

$$n = \int_{E_C}^{E_{C_{top}}} n(E)dE \approx \int_{E_C}^{\infty} N(E)F(E)dE \tag{2.1}$$

where $N(E)$ represents the density of states, $F(E)$ the Fermi-Dirac distribution function, E_C the bottom of the conduction band and $E_{C_{top}}$ the top of conduction band:

$$N(E) = 4\pi \left(\frac{2m_n}{h^2}\right)^{3/2} (E)^{1/2} \tag{2.2}$$

$$F(E) = \frac{1}{1 + e^{(E-E_F)/kT}} \tag{2.3}$$

The symbols used in (2.2) and (2.3) are the kinetic energy of electrons E, the Fermi level E_F, the Boltzmann constant k, the Planck constant h, the temperature T and finally the effective electron mass m_n that can be calculated as the second derivative of energy E with respect to the momentum p.

After the substitution of (2.2) and (2.3) into the quantity (2.1) and evaluation of the integral, we will obtain the concentration of electrons:

$$n = N_C \, e^{-(E_C - E_F)/kT} \tag{2.4}$$

where N_C is the effective density of states:

$$N_C = 2 \left(\frac{2\pi m_n kT}{h^2}\right)^{3/2} \tag{2.5}$$

Similarly, we can calculate the hole concentration:

$$p = N_V e^{-(E_F - E_V)/kT} \tag{2.6}$$

where E_V denotes the top of valence band and N_V the effective density of states:

$$N_V = 2 \left(\frac{2\pi m_p kT}{h^2}\right)^{3/2} \tag{2.7}$$

For silicon at room temperature (300 K) $N_C = 2.86 \times 10^{19}\,\mathrm{cm}^{-3}$ and $N_V = 2.66 \times 10^{19}\,\mathrm{cm}^{-3}$ [21].

From the relations (2.4), (2.6) and the fact that the number of holes and electrons per unit volume is the same ($n = n_i = p$), the intrinsic Fermi level can be calculated as:

$$E_F = E_i = \frac{E_C + E_V}{2} + \frac{3kT}{4} \ln \frac{m_p}{m_n} \tag{2.8}$$

At room temperature, the second term is much smaller than the first one. And thus the intrinsic Fermi level can be considered that lies almost in the middle of a band gap area.

Finally, if we take into account that:

$$np = n_i^2 \tag{2.9}$$

and the band gap energy will be rewritten into following form $E_g = E_C - E_V$ ($E_g = 1.12\,\mathrm{eV}$), one gets the intrinsic carrier density as:

$$n_i = \sqrt{N_C N_V} e^{-\frac{E_g}{2kT}} \tag{2.10}$$

Putting in numbers, the relation yields $n_i = 1.08 \times 10^{10}\,\mathrm{cm}^{-3}$.

For extrinsic semiconductors of following density of donors N_D, resp. acceptors N_A, there is enough thermal energy at room temperature to ionize all donor, resp. acceptor, impurities. Under this condition, called complete ionization, we can rewrite the electron density as $n = N_D$, resp. $p = N_A$, and calculate from (2.4), resp. (2.6), a new value of Fermi level:

$$E_C - E_F = kT \ln (N_C/N_D) \tag{2.11}$$

resp.:

$$E_F - E_V = kT \ln (N_V/N_A) \tag{2.12}$$

From these relations, it can be seen that the bigger the concentration of impurities is, the closer to the conduction band, resp. the valence band, the Fermi level is. Needless to say that effective densities are substantially higher than densities of dopants.

Further, it is useful to rewrite for extrinsic semiconductors the relations (2.4) and (2.6) for electron and hole densities into following form:

$$\begin{aligned} n &= N_C\, e^{-(E_C - E_F)/kT} = N_C\, e^{-(E_C - E_i + E_i - E_F)/kT} \\ &= n_i\, e^{(E_F - E_i)/kT} \end{aligned} \tag{2.13}$$

$$\begin{aligned} p &= N_V\, e^{-(E_F - E_V)/kT} = N_V\, e^{-(E_F - E_i + E_i - E_V)/kT} \\ &= n_i\, e^{(E_i - E_F)/kT} \end{aligned} \tag{2.14}$$

Note that the product of n and p still equals n_i^2. The result is identical to that for intrinsic case, see (2.9), and is called the mass action law.

If both donor and acceptor impurities are present simultaneously, the type that is present in greater concentration will determine the features of material and the type of conductivity. If we solve in such a case relation (2.9) under complete ionization condition, i.e.:

$$n + N_A = p + N_D \tag{2.15}$$

we will get the equilibrium electron and hole concentration in an n-type, resp. p-type, semiconductor:

$$n = 1/2 \left[N_D - N_A + \sqrt{(N_D - N_A)^2 + 4n_i^2} \right] \tag{2.16}$$

$$p = 1/2 \left[N_A - N_D + \sqrt{(N_D - N_A)^2 + 4n_i^2} \right] \tag{2.17}$$

2.3 Carrier Transport Phenomena

For semiconductor materials various transport phenomena are at work. The most important are the drift, the diffusion process and the movement in magnetic field.

The term drift means the movement of electrons, resp. holes, under the influence of external electric field $\vec{E}$. At low electric intensities, the drift velocity is linearly proportional to the applied field:

$$\vec{v} = \mp \mu \vec{E} \tag{2.18}$$

and the coefficient μ, the mobility of carriers, is constant.

As long as the applied field approaches higher values ($\sim 10^4\,\mathrm{Vcm}^{-1}$), the velocity dependence on the intensity begins to depart from the linear relationship and for sufficiently strong fields, the drift velocity becomes saturated.

For the region where the mobility of electrons, resp. holes, is dependent on the electric field, applied along $\langle 111 \rangle$ direction, following parametrization can be used [13]:

$$\mu = \frac{v_m / E_C}{(1 + (E/E_C)^\beta)^{1/\beta}} \tag{2.19}$$

where the values and temperature dependence ($T \geq 250\,\mathrm{K}$) of the parameters v_m, E_C and β are shown in tab. 2.1.

The diffusion process is caused by existence of spatial variations of carrier distribution. Both electrons and holes tend to move from a region of high

Parameter	Electrons	Holes	Units
v_m	$1.53 \times 10^9 \times T^{-0.87}$	$1.62 \times 10^8 \times T^{-0.52}$	$\mathrm{cm.s^{-1}}$
E_C	$1.01 \times T^{1.55}$	$1.24 \times T^{1.68}$	$\mathrm{V.cm^{-1}}$
β	$2.57 \times 10^{-2} \times T^{0.66}$	$0.46 \times T^{0.17}$	

Tab. 2.1: Parameters for the electric field and temperature dependence of electron and hole mobilities in high-purity silicon

concentration to a region of low concentration and create thus the diffusion flux that can be expressed as:

$$\vec{F} = -D\vec{\nabla}n \tag{2.20}$$

where D is called the diffusion coefficient or diffusivity and is related to the mobility by the Einstein relation:

$$D = \frac{kT}{q}\mu \tag{2.21}$$

q denotes an elementary charge and T the temperature.

The movement in a magnetic field $\vec{B}$ results in the change of direction by a Lorentz angle ϑ_L:

$$\tan\vartheta_L = \mu_H B \tag{2.22}$$

The coefficient μ_H is called the Hall mobility.

2.4 The P-N junction

The basic structure used in detector physics is the p-n junction. Its main characteristic is that it allows current to flow in only one direction. The p-n junction is obtained by joining together two extrinsic semiconductors of opposite doping. After both types are put together, created gradient of concentration causes carrier diffusion. The holes begin to diffuse from the p-side into the n-side and the electrons from the n-side to the p-side. Since the acceptor ions (N_A^-) are fixed, uncompensated negative space charge in p-region near the junction will be formed. Similarly the uncompensated donor ions (N_D^+) will form positive space charge in n-region. The total created space charge results in an existence of electric field $\vec{\mathcal{E}}$ in the direction opposite to the diffusion current and an equilibrium between the drift and the diffusion

will be formed. The result can be for holes rewritten as:

$$\begin{aligned} j &= j_{\text{diffusion}} + j_{\text{drift}} = 0 \\ &= qv_p p - qD_p \frac{dp}{dx} \\ &= q\mu_p \vec{\mathcal{E}} p - kT\mu_p \frac{dp}{dx} \\ &= q\mu_p p \left(\frac{1}{q} \frac{dE_i}{dx} \right) - kT\mu_p \frac{dp}{dx} \end{aligned} \tag{2.23}$$

where (2.20), (2.21) and the fact, that the current density can be expressed as the product of elementary charge, velocity and carrier density, have been used. One more remark is in order here. The relation between el. intensity and intrinsic Fermi level:

$$\mathcal{E} = -\frac{d\varphi}{dx} = \frac{1}{q} \frac{dE_i}{dx} \tag{2.24}$$

can be get from the following idea: since the applied voltage to a semiconductor causes the shift of potential energies and the same shift of band energy levels, any of these levels can be identified with the electrostatic potential. For instance, the intrinsic Fermi level.

Substituting expression (2.14) and its first derivative into (2.23), one get the condition for p-n junction at thermal equilibrium, the Fermi level must be constant:

$$\frac{dE_F}{dx} = 0 \tag{2.25}$$

The same condition can be get for electron current density.

The constant Fermi level results in a unique space charge distribution that is related to the electrostatic potential by Poisson's equation:

$$\frac{d^2\varphi}{dx^2} \equiv -\frac{d\mathcal{E}}{dx} = -\frac{\rho}{\varepsilon} = -\frac{q}{\varepsilon}(N_D - N_A + p - n) \tag{2.26}$$

In regions, far away from the junction, charge neutrality is conserved and the total charge density ρ is zero. From (2.14), (2.24) and under the conditions $N_D = 0$ and $N_A = \text{const.} = p \gg n$ we will get the potential of p-type region, with respect to the Fermi level:

$$\varphi_p \equiv -\frac{1}{q}(E_{i_p} - E_F) = -\frac{kT}{q} \ln \left(\frac{N_A}{n_i} \right) \tag{2.27}$$

In the same way one can get the electrostatic potential of n-type region, with respect to the Fermi level:

$$\varphi_n \equiv -\frac{1}{q}(E_{i_n} - E_F) = \frac{kT}{q} \ln \left(\frac{N_D}{n_i} \right) \tag{2.28}$$

The total difference between n-side el. potential and p-side el. potential is called built-in potential:

$$V_{bi} = \varphi_n - \varphi_p = \frac{kT}{q} \ln\left(\frac{N_A N_D}{n_i^2}\right) \tag{2.29}$$

and the region where the majority carriers are missing and the potential barrier V_{bi} is created is called depletion area.

The total length of depletion area $W = x_p + x_n$ can be calculated by solving the Poisson's equation separately for p-region of length x_p and carrier concentration N_D = const. and for n-region of length x_n and carrier concentration N_A = const.:

$$\frac{d^2\varphi}{dx^2} = -\frac{q}{\varepsilon}(N_A) \quad \text{for} \quad -x_p \leq x < 0 \tag{2.30}$$

$$\frac{d^2\varphi}{dx^2} = -\frac{q}{\varepsilon}(N_D) \quad \text{for} \quad 0 < x \leq x_n \tag{2.31}$$

The overall space charge neutrality of the whole junction requires that the total density of space charge in n-type must be precisely equal to the total density of space charge in p-type.

$$N_A x_p = N_D x_n \tag{2.32}$$

Under this condition and the condition that the first derivative of electric potential should be zero for $x = -x_p$ and $x = x_n$, the electric field is obtained by integrating (2.30) and (2.31):

$$\mathcal{E} = -\frac{d\varphi}{dx} = -\frac{qN_A(x + x_p)}{\varepsilon} \quad \text{for} \quad -x_p \leq x < 0 \tag{2.33}$$

$$\mathcal{E} = -\frac{d\varphi}{dx} = \frac{qN_D(x - x_n)}{\varepsilon} \quad \text{for} \quad 0 < x \leq x_n \tag{2.34}$$

After next integration over the whole depletion area is performed, the built-in potential will be obtained:

$$V_{bi} = -\int_{-x_p}^{x_n} \mathcal{E}dx = -\int_{-x_p}^{0} \mathcal{E}dx - \int_{0}^{x_n} \mathcal{E}dx = \frac{qN_A x_p^2}{2\varepsilon} + \frac{qN_D x_n^2}{2\varepsilon} \tag{2.35}$$

Finally, the combination of (2.32) and (2.35) gives the depletion width:

$$W = \sqrt{\frac{2\varepsilon}{q}\left(\frac{N_A + N_D}{N_A N_D}\right) V} \tag{2.36}$$

From the relation it can be easily seen that if one applies external reverse voltage ($V = V_{bi} + V_{extrev}$), $V_{extrev} > 0$, the depleted region of junction will be extended and an area without majority carriers created. This mechanism forms the basic principle of detectors based on a diode effect, e.g. semiconductor microstrip detectors. But an important remark has to be made here. The preceding relations are only valid for abrupt junction, i.e. N_D and N_A are constant. In opposite case the relations would be more complicated.

Another important characteristic is a depletion capacitance C. The capacitance is related to an increment of charge $dQ = qNdW$ created on both sides of the junction after the change of external voltage:

$$C = \frac{dQ}{dV} = \frac{dQ}{dW}\frac{dW}{dV} = \frac{\varepsilon}{W} \quad \mathrm{F/cm^2} \tag{2.37}$$

In the end, the drift time of electrons, respectively holes, will be found. All calculations will be made for simple abrupt p-n junction (length=d) with higly doped and constant p-side, denoted as p^+, and moderately doped and constant n-side. The whole structure will be used in overdepleted mode, i.e. the external voltage will be given as a sum of voltage needed for depletion and extra added voltage $V = V_{dep} + V_{extra}$. The electric intensity will be then given as a sum of intensity expressed from the relation (2.34) under following condition $d \equiv W \approx x_n \approx \sqrt{\frac{2\varepsilon}{q}\frac{V}{N_D}}$ and intensity due to extra voltage:

$$\begin{aligned} \mathcal{E} &= -\frac{2V_{dep}}{d^2}(d-x) - \frac{(V - V_{dep})}{d} \\ &= -\left(\frac{V + V_{dep}}{d} - \frac{2x}{d^2}V_{dep}\right) \end{aligned} \tag{2.38}$$

If one knows the intensity, the position of electrons, resp. holes, can be easily calculated from these differential equations, see (2.18):

$$\begin{aligned} \frac{dx_e}{dt} &= \mu_e\left(\frac{V + V_{dep}}{d} - \frac{2x_e}{d^2}V_{dep}\right) \\ \frac{dx_h}{dt} &= -\mu_h\left(\frac{V + V_{dep}}{d} - \frac{2x_h}{d^2}V_{dep}\right) \end{aligned} \tag{2.39}$$

After the simple method of integration in separated variables is used (with following boundary conditions: $x_e = x_h = x$ at $t = 0$), one will get the electron, resp. hole, positions:

$$\begin{aligned} x_e(t) &= \frac{d}{2}\frac{(V + V_{dep})}{V_{dep}} + \left(x - \frac{d}{2}\frac{(V + V_{dep})}{V_{dep}}\right)e^{-\mu_e\frac{2}{d^2}V_{dep}t} \\ x_h(t) &= \frac{d}{2}\frac{(V + V_{dep})}{V_{dep}} + \left(x - \frac{d}{2}\frac{(V + V_{dep})}{V_{dep}}\right)e^{\mu_h\frac{2}{d^2}V_{dep}t} \end{aligned} \tag{2.40}$$

Finally, the drift time is obtained after simple operations with preceding relations, when taking that a carrier is stopped after it reaches an electrode:

$$\begin{aligned} t_e &= \frac{d^2}{2\mu_e V_{dep}} \ln\left(\frac{V+V_{dep}}{V-V_{dep}}\left(1-\frac{2x}{d}\frac{V_{dep}}{V+V_{dep}}\right)\right) \\ t_h &= -\frac{d^2}{2\mu_h V_{dep}} \ln\left(1-\frac{2x}{d}\frac{V_{dep}}{V+V_{dep}}\right) \end{aligned} \tag{2.41}$$

2.5 Light Absorption in Silicon

Light beam, resp. laser beam, incident at a certain angle on material surface is partially reflected and partially refracted into silicon. The relation between an angle of incidence θ_{inc} and an angle of refraction θ_{refr} is given by Snell's law:

$$\frac{\sin(\theta_{inc})}{\sin(\theta_{refr})} = \frac{n_{Si}}{n_{in}} \tag{2.42}$$

where n_{in} denotes a refractive index of input material and n_{Si} a refractive index of output material, i.e. silicon.

The intensity I of transmitted part of the light beam is gradually attenuated as the beam is traversing the material. The attenuation is exponential:

$$I = I_{trans} \exp(-\alpha x) \tag{2.43}$$

and the mean rate of attenuation is given by the absorption coefficient α, a parameter that expresses how far, i.e. x, into the material an incident photon will travel before being absorbed by the lattice and creating electron-hole pair. Due to the fact that silicon represents indirect semiconductor, i.e. the creation of e-h pairs must be accompanied by lattice interaction, the photon energy must be higher than the value of band gap to be absorbed.

The absorption coefficient as well as the refractive index can be calculated from the analytical model described in detail in [15]. For 1060 nm laser, the refractive index has been calculated as $n_{refr} = 3.554$ and the attenuation length equal to the inverse value of α as $\lambda_{att} = 894.2\,\mu$m.

2.6 Interactions of Particles in Silicon

Ionization and excitation, resp. bremsstrahlung, form two basic mechanisms of energy losses of a charged particle in solid matter. For heavy particles mainly the first one is substantial, for light particles, e.g. electrons, both of them play an important role. Here, only ionization and excitation will be discussed in detail.

The mean rate energy loss due to ionization can be described by Bethe-Bloch formula [16]:

$$-\frac{1}{\rho}\left\langle\frac{dE}{dx}\right\rangle_{ion} = Kz^2\frac{Z_{med}}{A_{med}}\frac{1}{\beta^2}\left[\frac{1}{2}\ln\frac{2m_ec^2\beta^2\gamma^2T_{max}}{I^2} - \beta^2 - \frac{\delta}{2}\right] \tag{2.44}$$

where T_{max} is the maximum kinetic energy:

$$T_{max} = \frac{2m_ec^2\beta^2\gamma^2}{1 + 2\gamma m_e/M + (m_e/M)^2} \tag{2.45}$$

which can be imparted to a free electron in a single collision and δ represents the correction to the density effect. (The electric field of an incident particle results in polarisation of individual atoms of material, which in turn shield the electric field of the particle.) Other variables are defined in tab. 2.2.

Variable	**Definition**	**Value or Unit**
ze	incident particle charge	
M	incident particle mass	$\mathrm{MeV/c^2}$
β	incident particle velocity in $c = 1$	
	$\sqrt{1-\gamma^{-2}}$	
T	kinetic energy	MeV
m_e	electron mass	$511\,\mathrm{keV/c^2}$
r_e	classical electron radius	$2.818\,\mathrm{fm}$
	$e^2/4\pi\varepsilon_0 m_e c^2$	
N_A	Avogadro's number	$6.022\times10^{23}\,\mathrm{mol^{-1}}$
Z_{med}	atomic number of absorber	
A_{med}	atomic mass of absorber	g/mol
ρ	absorber density	$\mathrm{g/cm^3}$
K	$4\pi N_A r_e^2 m_e c^2$	$0.307\,\mathrm{MeVcm^2}$
I	mean excitation energy	eV
	$\approx 16.Z^{0.8}$	

Tab. 2.2: Summary of variables used in this section

Due to stochastic nature of energy losses, large statistical fluctuations can occur in the amount of energy deposited by the particle in material. The character of ionization fluctuations can be described by the significance parameter κ that is expressed as the ratio of mean energy loss ξ to the maximum possible energy transfered in a single collision:

$$\kappa = \frac{\xi}{T_{max}} \tag{2.46}$$

If almost all the energy of the incident particle traversing the material is deposited, i.e. ($\kappa > 10$), the Gaussian distribution can be used for description of fluctuations. In the opposite case, the particle deposits only a part of its energy in material and for ($10 \geq \kappa > 0.01$) the Vavilov distribution should be used and for ($0.01 < \kappa$) the Landau distribution should be used. But Landau formalism has another restriction: the typical energy loss in the absorber should be large compared to the binding energy of the most tightly bound electron. It means that the low energy transfers must be high enough with respect to I ($\xi/I \sim 50$). Below this limit special models taking into account the atomic structure of material should be taken. In general, the validity range of the Landau theory depends on the type and energy of the particle, Z_{med}, A_{med} and the ion. potential I. More information can be found in [12] and [23]. For MIP and typical thickness ($\approx 300\,\mu$m) of silicon detectors it has been found that the Landau distribution is not adequate for description of energy loss and thus special model, photoabsorption ionization model (PAI model), has to be used. By way of illustration, two detailed simulations in Geant 3 with 8 GeV/c pion traversing 290 μm thick silicon bulk has been made and compared to real data cited in [7]. The result is in fig. (2.1): the black solid line corresponds to PAI model, blue dashed line to Landau

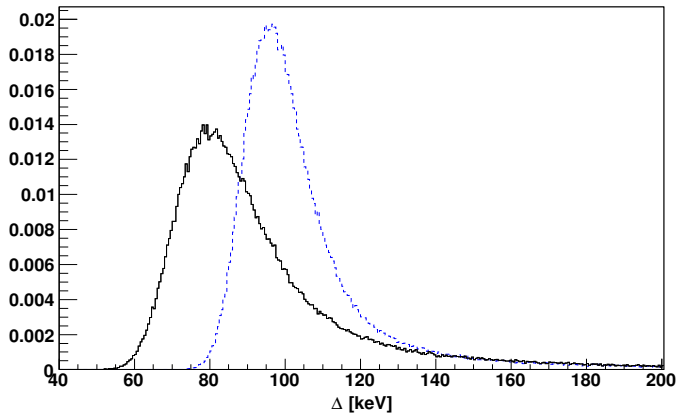

Fig. 2.1: Energy loss distributions of 8 GeV/c π^- in 290 μm thick silicon material. The black solid line corresponds to PAI model, the blue dashed line to Landau distribution.

theory. If we compare the results with experimental values:

	PAI model	**Landau distr.**	**Experiment**
MPW $\left\langle \frac{dE}{dx} \right\rangle$ [keV]	79 ± 1	96 ± 1	79.43
width w [keV]	29 ± 1	20 ± 1	29.24

we can see that the MPW[2] of Landau distribution is slightly shifted and the width is narrower than it should be. The PAI model corresponds in perfect way.

An important part of ionization process is production of high-energy electrons (δ-rays). The δ-electrons have an important influence on the distribution of statistical fluctuations of energy loss. Particularly the tail of distribution is caused by high-energy electrons. For a relatistivic particle the number of created δ-electrons produced per cm and with kinetic energy higher than a certain value ($T > T_{cut}$) can be estimated as [23]:

$$\frac{dN}{dx} \approx \frac{K\rho}{2}\frac{Z_{med}}{A_{med}}\frac{z^2}{T_{cut}} \tag{2.47}$$

This formula is valid for electrons as well as for other particles.

The δ-electron with momentum p_δ and kinetic energy T_δ is produced at angle [16]:

$$\cos\theta_\delta = \frac{T_\delta}{p_\delta}\frac{p_{max}}{T_{max}} \tag{2.48}$$

2.7 Silicon Microstrip Detectors

The silicon microstrip detector is based on a physical principle of a reverse biased p-n junction working in overdepleted mode. It primarily consists of p^+ strips implanted in n-type bulk with $< 111 >$ orientation. Another components are the aluminium strips that serve as good ohmic contacts between p^+ layer and n-type substrate, aluminium backside and n^+ layer. In order to keep the strips implants at a defined potential, i.e. grounded, the aluminium strips are connected through a poly-silicon bias resistance R_{bias} to a common grounding rail. The bias voltage that holds the detector depleted is connected to the backside. Since the detector is designed to stand high voltage, special guard rings are used to step down the voltage towards the edge of the detector. The purpose of n^+ layer is twofold: it allows to operate in overdepleted mode and simultaneously provides good ohmic contact from aluminium to the substrate. In order to illustrate the typical geometry of the detector, the cross section of a microstrip detector is shown in fig. 2.2.

Except for the layout of the detector, the schematic diagram of capacative connections is depicted in the picture. The most important capacitance, coupling capacitance C_c, is implemented between the strips and the front end electronics. It effectively enables to avoid the DC load caused by continuously generated leakage currents. The intrinsic capacitance of the detector

[2]The most probable value of energy loss

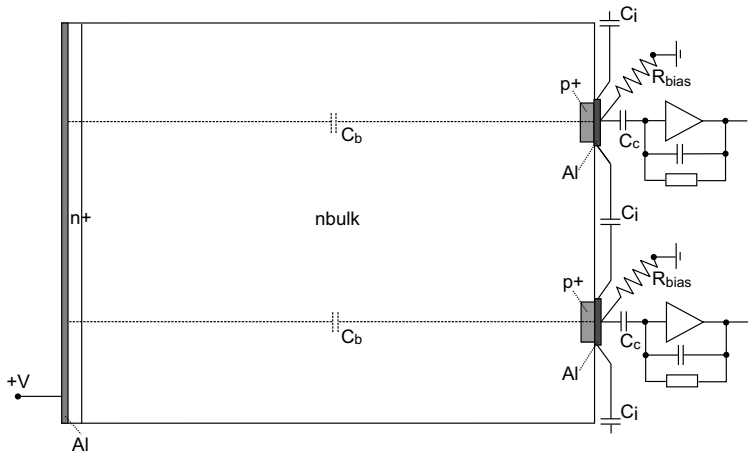

Fig. 2.2: Silicon Microstrip Detector Layout

C_b, i.e. between the strip and the backside, represents the capacitance of p-n junction. It characterizes whether the detector is fully depleted when changing the total voltage. The interstrip capacitance C_i is significant when taking into account the charge sharing among the strips. Such a redistribution of a signal is called the strip cross talk and the strength of the effect is strongly dependent on the metallisation layer.

If we want to estimate the fraction of the signal that is induced on a neighbouring strip due to cross talk, we can use this relation:

$$i_{\text{nstrip}} = \frac{i_{\text{strip}} C_i}{C_b + C_c + C_i} \tag{2.49}$$

The relation is obtained from the following idea: the ratio of electric current flowing from the strip to its electronics and the current flowing from the same strip to the electronics on the left side, for instance, is estimated as the reverse ratio of impedances of individual branches, i.e. the branch between the strip and the electronics and the branch connecting the strip with the electronics on the left side. If we put that into equations and ignore the impedance of the amplifier, the result above is easily obtained.

For SCT detectors the binary read-out system is used. The signal induced on a strip and preprocessed by front end electronics is compared to a given threshold and a binary result (0×1) is obtained. The measurement precision Δx^2 for such detectors depends mainly on the strip pitch p and can be calculated as:

$$\left\langle \Delta x^2 \right\rangle = \frac{1}{p} \int_{-p/2}^{+p/2} x^2 dx = \frac{p^2}{12} \tag{2.50}$$

As the detector contains two mutually rotated microstrip wafers, the position measurement is in fact more accurate .

For the overall performance of microstrip detector the noise characteristics are essential. There are two contributions to the noise, one from the front end electronics, the other from detector capacitances. The noise of a front end system can be written as the quadratic sum of two contributions: thermal noise due to variations in the velocities of charge carriers and shot noise that is a result of the fact that the current consists of discrete quanta of charge. The noise coming from the capacitances is mainly given by the interstrip capacitance and the capacitance between the backplane and the strip.

In the next chapter the response of a barrel detector will be simulated. Therefore, it's useful to summarize the parameters of SCT barrel modules (Hamamatsu) in following tab. 2.3.

Variable	**Definition**	**Value**
d	detector thickness	$285\,\mu$m
p	detector pitch	$80\,\mu$m
w	p^+ width	$16\,\mu$m
	aluminium width	$22\,\mu$m
h	p^+ height	$\approx 1 - 1.5\,\mu$m
	aluminium height	$\approx 1\,\mu$m
N_D	density of donors	$\approx 10^{12}\,\mathrm{cm}^{-3}$
N_A	density of acceptors	$\approx 3 \times 10^{19}\,\mathrm{cm}^{-3}$
V	external bias voltage	150 V
n_{refr}	refraction index for $\lambda = 1060\,$nm	3.554
λ_{att}	attenuation length for $\lambda = 1060\,$nm	$894.2\,\mu$m
C_i	interstrip capacitance	6 pF
C_b	detector capacitance	1.7 pF
C_c	coupling capacitance	120 pF
ENC	equivalent noise charge	$\approx 1500\,$e
V_{bi}	internal bias voltage	0.68 V
V_{dep}	voltage needed for full depletion	61 V
C_b	calculated det. capacitance	1.77 pF
t_e	drift time limit for an electron	14.7 ns
t_h	drift time limit for a hole	6.1 ns

Tab. 2.3: The parameters of SCT barrel detector

The bias voltage V_{bi} has been calculated from (2.29), the depletion voltage V_{dep} from the depletion width d, i.e. the thickness of the detector, (2.36),

the detector capacitance C_b from (2.37) and the limits for the drift times of e-h pairs distributed between the strip and the backside from relation (2.41). (The mobility has been evaluated at room temperature from (2.19) and the intensity between the strip and the backplane has been estimated as the intensity of a plate capacitor.)

3 SCT Simulations

In this chapter the simulation of charge collection in a silicon microstrip detector will be explained. Further, the focus will be given on Geant 3 framework that has been used for simulation of energy loss of a particle passing through the detector. And at last the Monte Carlo results will be discussed. Detailed description of the program based on conception of Mazziotta and Loparco [13] can be found in Appendix A.

3.1 Signal Simulation

After an ionizing particle crosses the detector volume, e-h pairs are created along its path. In order to simulate the drift of charge carriers inside the silicon material, a detailed map of the electric potential and consequently the electric field has to be evaluated. It has been done by dividing the detec-

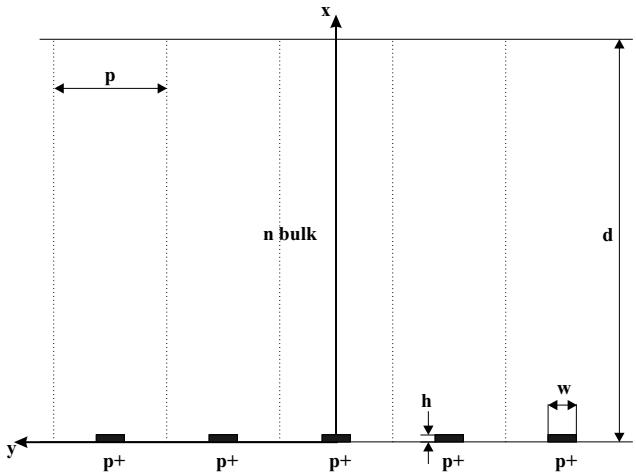

Fig. 3.1: Schematic layout of detector geometry. The reference system is located in such a way that the coordinate x passes through the center of a strip and the coordinate y the edge of detector. The boundaries of elementary cells are represented as dotted lines.

tor volume, using the periodic structure, into elementary cells (see fig. 3.1) and solving the Poisson's equation in a half of a single cell:

$$\triangle\varphi = -\frac{\rho}{\varepsilon} \tag{3.1}$$

The solution is then extended into second half using odd symmetry of the field. The boundary conditions has been set as:

$$\begin{aligned} &\varphi(x = 0, -w/2 \leq y \leq w/2) = 0 \\ &\varphi(x = d) = V \\ &\varphi(y = -p/2) = \varphi(y = p/2) \end{aligned} \tag{3.2}$$

and imply that the backside is connected to the defined value of potential and the strip is grounded. Another condition results from the periodic structure of a detector. In a depleted region a fixed charge density ρ has been assumed. Its value can be practically calculated from the condition of the overall space charge neutrality (2.32), if we take into account the thickness of the detector, i.e. the depletion width, and approximate width of p^+ layer. For more details see section 2.4.

The electric potential, resp. the electric field, has been evaluated on a two dimensional discrete mesh by using MAXWELL 2D package [1] for a Hamamatsu barrel detector. Its parameters are summarized in tab. 2.3. Still one more remark: a uniform doping of n bulk, resp. p^+ implant, has been assumed. The potential is depicted in fig. 3.2. The electric intensities

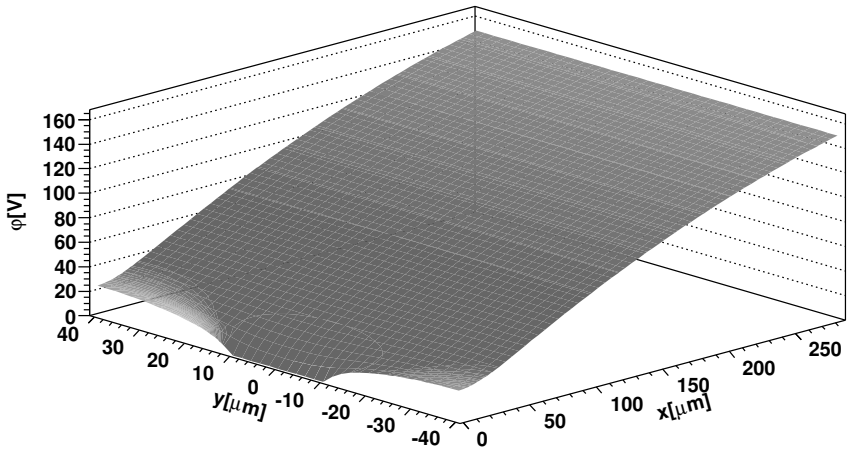

Fig. 3.2: Electric potential φ in an elementary cell.

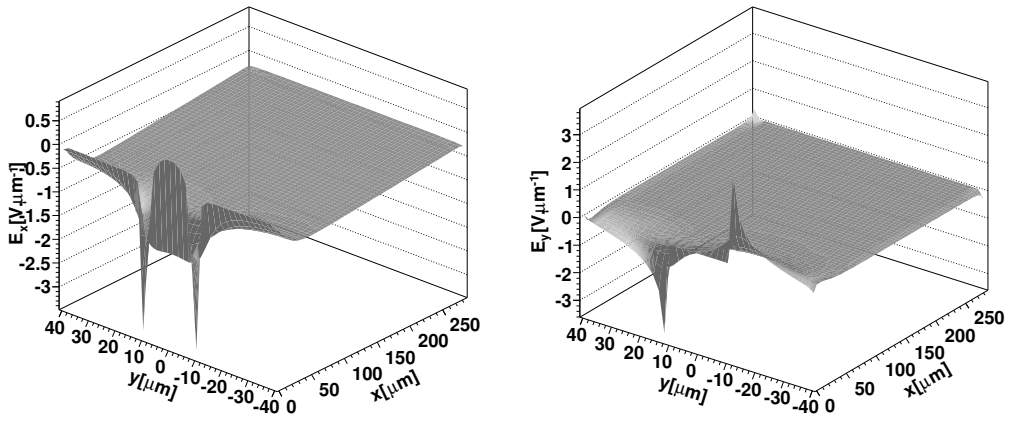

Fig. 3.3: Electric intensity E_x in direction x and electric intensity E_y in direction y evaluated in an elementary cell. The strip is located at $y = 0$.

are shown in figure 3.3.

Under the action of electric field the electrons will drift to the backside and the holes to the strip. To simulate the signal induced on the electrodes due to the motion, we have to solve separately for each hole and each electron the first order differential equation of motion (2.18), described in previous chapter. Since the charge mobility is strongly dependent on electric intensity (see (2.19)), the equation of motion has to be solved numerically, using the classical fourth-order Runge-Kutta method. (An excellent explanation of this method is given in [17].) Ideally, the integration time step size δt should be adjusted so that the accuracy of simulation would be high enough not to lose a part of the signal. On the other hand the CPU resources are limited and an optimal value has to be found.

The simulation has been practically realized in following way: for each integration step first the position of a carrier has been found, then the intensity of electric field at this position has been evaluated, further an actual velocity from relation (2.18) has been calculated and finally, the time step size δt according to the formula:

$$\delta t = \frac{\varepsilon}{|\vec{v}\,(\vec{r}(t))|} \tag{3.3}$$

has been calculated, where ε denotes the optimal simulation space accuracy and $\vec{v}$ the velocity. For $285\,\mu$m thick detector the optimal value of accuracy has been found $5\,\mu$m. In the area, where the potential changes rapidly and the accuracy must be higher not to lose a signal the value has been set 10 times smaller there.

During the drift still another effect influences the motion of electrons, respectively holes, and thus, has to be taken into account – the diffusion. The created electrons, resp. holes, are diffused during the motion by multiple collisions. After time t the distribution of charge carriers is changed due to this effect. The new distribution is described by Gaussian law:

$$dN = \frac{N}{\sqrt{4\pi D t(\vec{r})}} \exp\left(-\frac{\vec{r}^2}{4Dt(\vec{r})}\right) d\vec{r} \tag{3.4}$$

where dN/N denotes the fraction of carriers in an element $d\vec{r}$ at distance $\vec{r}$ from the track. The variable D is described in section 2.3.

The total simulation step is then given as a sum of two terms: the step due to the drift evaluated with Runge-Kutta method and the step due to a random diffusion effect given by Gaussian law.

$$\delta\vec{r} = \delta\vec{r_{\text{drift}}} + \delta\vec{r_{\text{diffus}}} \tag{3.5}$$

To recap, for each carrier first the drift step is evaluated, then the random diffusion step is generated according to the Gaussian distribution and finally a new position is calculated. If a carrier left after the step the detector volume, one has to verify if it resulted from a diffusion effect or from the drift. In the first case the diffusion step is repeated and once more the posititon check is made, in the latter case the carrier is stopped. Otherwise the next step is performed.

The current induced at time t on the kth electrode by a moving carrier has been evaluated from the Shockley-Ramo theorem [10] as:

$$i_k(t) = -q\vec{v} \cdot \vec{E_{wk}} \tag{3.6}$$

where q represents the charge of a carrier, $\vec{v}$ its velocity and $\vec{E_{wk}}$ the weighting field associated to the kth electrode. In general, the weighting field describes the geometrical coupling between a carrier at the position $\vec{r}$ and the electrode k. In current parlance, the effect caused by the weighting field is called the charge sharing effect and results in the following: even if the charge is still drifting, we can measure on electrodes the current induced by the carrier. Namely, not only on the electrode that the carrier is drifting to, but also on adjacent electrodes.

The weighting potential and consequently the weighting field have been calculated from the Laplace equation with these boundary conditions:

$$\begin{aligned} &\varphi_{wk}(x = 0, y = kp) = 1 \quad k = 0, \pm 1, \pm 2, \ldots \\ &\varphi_{wi}(x = 0, y = ip) = 0 \quad i \neq k \\ &\varphi_w(x = d) = 0 \end{aligned} \tag{3.7}$$

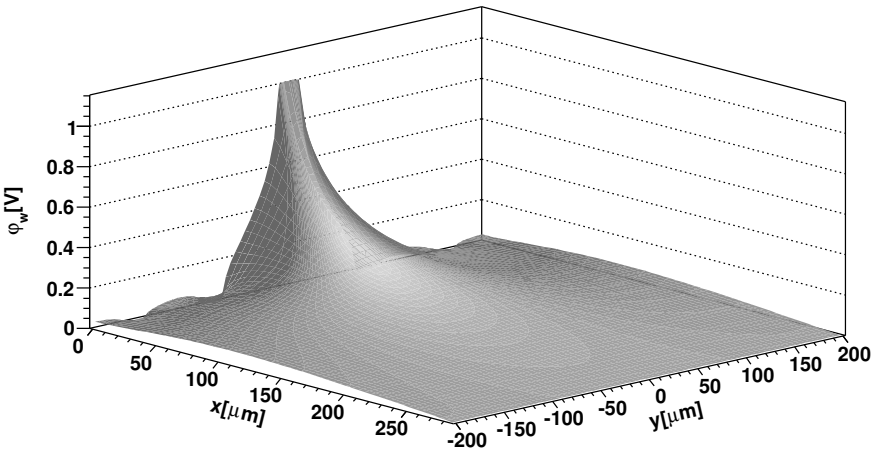

Fig. 3.4: Weighting potential φ_w of a strip at $y = 0$. The cell used for calculation includes in addition two strips on both sides.

Moreover, the solution, see fig. 3.4, has been calculated in a central cell including two adjacent cells on one side and then again symmetrically extended to the cells on the opposite side.

In order to get electric currents evaluated at constant time steps (in our case 0.25 ns), the induced currents are interpolated using Newton's Divided Difference Method of Interpolation [22].

3.2 Geant 3 Simulation

The Geant framework [23] is used for simulation of the passage of elementary particles through the matter. The system allows: to describe the geometry of experimental setup, in our case the silicon wafer, to simulate the transport of a defined particle through the various regions of the setup, taking into account the geometrical structure and the physical processes, that occur in the material, and finally, to record particle trajectories and the response of sensitive parts of a detector.

The experimental setup, where the particles are transported, is represented by a structure of geometrical volumes filled with matter. The matter is characterized by two sets of attributes. The first set corresponds to the nature of material: atomic number, the atomic weight, the density, the radiation length and the absorption length. The second set of attributes, such as: material sensitivity (In terminology of Geant 3 the detector material is

called sensitive to a particle, if the information about the particle is read-out. In our case only the wafer is a sensitive material.), magnetic field, electric field, max. permitted step, etc. This set of attributes is relevant to the process of particle transport. An initial volume inside which all other volumes will be positioned, i.e. inside which the detector structure will be defined, represents the "mother" volume and is naturally connected with the MAster Reference System (MARS) that all the kinematic variables are always referred to. The MARS is located at the center of the volume. Every other volume that will be positioned in the "mother" volume is called "daughter" and has its own reference system located at the center of the volume. If one wants to position "daughter" inside the "mother" volume, it will be done with respect to the MARS.

In our case, we have defined for simplicity only a rectangular silicon wafer without any supporting structure and electronics. The silicon wafer (6 cm $\times$6 cm$\times$285 μm) has been positioned inside a `BIGBOX` (7 cm$\times$7 cm$\times$0.1 cm), that corresponds to the above defined "mother" volume. The properties of silicon material have been taken from [16] and are summarized in tab. 3.1. Moreover, no electric field, resp. magnetic field has been defined.

Variable	**Definition**	**Value**
Z_{med}	Si atomic number	14
A_{med}	Si atomic weight	28.0855 g/mol
ϱ	Si density	2.33 g/cm^3
λ_i	Si nucl. interaction length	45.49 cm
X_0	Si radiation length	9.36 cm

Tab. 3.1: Silicon Material Properties

The simulation of the passage of a particle through the defined experimental setup is performed in Geant in following steps:

1. For the particle, that will be tracked, the number X of interaction lengths is randomly generated using the macroscopic cross section Σ. The number is generated for each process we want to include into the simulation.

2. The distance to the interaction point is evaluated. For each process X is multiplied by corresponding inverse macroscopic cross section, i.e. by the interaction length. This gives the distances that the particle has to travel before each of the processes occurs and the shortest distance is then taken as a simulation step.

3. Transportation of the particle is performed, either along a straight line, if no mag. field is defined or a neutral particle is transported, or along helicoidal path, if the detector is in mag. field.

4. Update of the particle energy is made, if continuous energy loss effect is required. If discrete physical processes have been selected, secondary particles are generated and, in our case, saved for next tracking.

5. If the incident particle survives the interaction, the number of interaction lengths for this process is sampled again.

6. Update of the number of interaction lengths for all selected processes is performed and the sequence from point 2 is repeated until either the particle leaves the detector volume or its energy falls bellow the set threshold or disappears in the interaction.

It has been found that, due to thinness of the wafer, the number of steps that the particle needs for crossing the silicon material is too low, to hold the required space accuracy of simulation ε. Therefore the maximal permitted step `STEMAX` has been decreased from the automatically calculated value to $5\,\mu$m and simultaneously the variable `IGAUTO` has been changed to zero. Only in such a case, the value `STEMAX` defining new properties of tracking medium is accepted as a true parameter. Moreover, if one changes the tracking parameters that are calculated in Geant implicitly, it has to be verified, that the change doesn't influence the physical results, we are interested in. Such comparison has been done and no visible change in energy loss distribution, that is crucial for simulation of detector response, has been seen.

According to a value of `ILOSS` variable a few alternatives are available in Geant to simulate the energy loss by an ionizing particle. In our case, especially two variants have been important: `ILOSS=2` and `ILOSS=1`. The first alternative results in continuous energy loss simulated according to the Landau, Vavilov or Gauss fluctuations (for more details see section 2.6) and without generation of δ-rays. The latter results in continuous energy loss with generation of δ-rays above the so-called cut, `DCUTE`, and with restricted Landau fluctuations below the cut. In Geant, in fact, the secondary particles are generated only, if their energy is above the set energy threshold T_{cut}, otherwise the particle is not produced and the energy is taken as deposited in the material. For δ-rays generated by electrons and positrons the cut is denoted as `DCUTE` and for δ-rays generated by other particles as `DCUTM`. The value of the cuts have been set for `ILOSS=2` to 10 TeV, i.e. to the highest possible limit, and for `ILOSS=1` to the value of energy cut, above which

an electron will be in electromagnetic interactions generated, to `CUTELE`. Its value has been set to 10 keV. In order to simulate gammas from the lowest possible cut, the `CUTGAM` has been also set to 10 keV.

For the simulation of barrel detector response both of the regimes have been used. The first alternative has been used for simple simulation without δ-electrons and with the step calculated automatically (The energy has been then divided uniformly along the track with the step ε.), the second has been used for more detailed simulation with δ-electrons and with the maximal permitted step set. (The energy has been then taken in the way exactly as deposited.) Still one more remark is in order here, due to fact mentioned in section 2.6, more sophisticated model taking into account the structure of material, the so-called PAI model, has been used for energy loss fluctuations instead of default models. The comparison of energy loss distributions for the two approaches is shown in fig. 3.5.

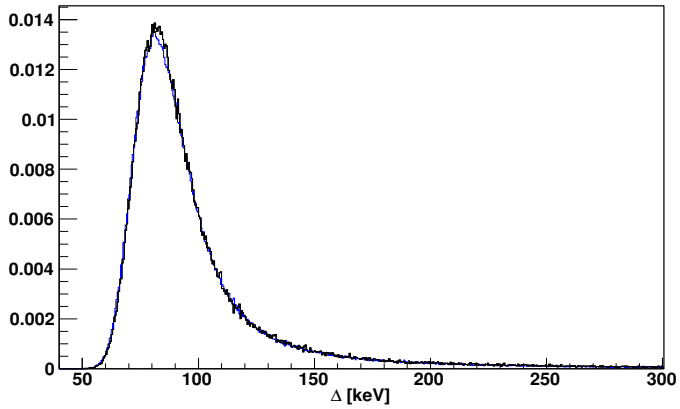

Fig. 3.5: Comparison of energy loss distributions for 180 GeV/c π^- in 285 μm thick silicon bulk. The black line corresponds to simulation with δ-electrons and with the `STEMAX` set to 5 μm, the blue line to simulation without δ-electrons and with automatically calculated step. The median value can be evaluated for both as (89.0 ± 0.5) keV.

After a map of deposited energy has been evaluated, the transformation of coordinates from the Geant reference system to the reference system defined in the simulation of charge collection has been performed and finally, the simulation of charge carriers propagation has been started.

3.3 Monte Carlo Results

In order to show, how for a certain detector geometry individual physical effects influence the results, we have simulated the response of Hamamatsu detector to 180 GeV/c pions incident at zero angle. (The temperature of a silicon wafer has been set to $T = 300$ K.) The strength of particular effects can be shown by means of the so-called η function that represents a very sensitive variable to an influence of charge sharing effect, diffusion, cross talk and δ-electrons. For a particle crossing the detector randomly in a region between two strips the η function is defined as:

$$\eta = \frac{q_{\text{left}}}{q_{\text{left}} + q_{\text{right}}} \tag{3.8}$$

where q_{left}, resp. q_{right}, represent the collected charge on the left strip, resp. the right strip. In our case, we had not simulated for simplicity the influence of electronics, so that the η function is calculated from the collected charge only and not from the voltage that will be obtained in real detectors.

The simulated η function (10 000 events) is depicted in fig. 3.6. The dot-

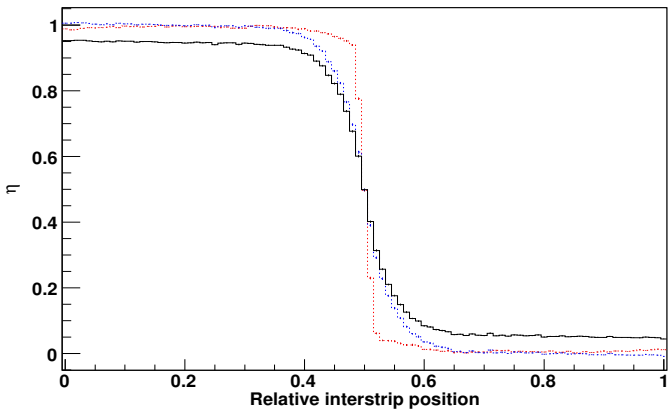

Fig. 3.6: Simulated η function for a sample of 180 GeV/c π^- crossing the detector at zero angle. The results are shown dependent on various physical effects: only an effect of weighting field is included (dotted red line), effects of weighting field together with diffusion are included (dotted blue line), all mentioned effects are included together with cross talk (solid black line).

ted red line corresponds to the effect of weighting field, the dotted blue line to the common effect of weighting field and diffusion process and the black line to the sum of all particular effects: weight. field effect, effect of diffusion and

cross talk. The cross talk (see section 2.7) has been evaluated in the following way: From the relation (2.49), using the detector parameters from tab. 2.3, it has been calculated that for each strip $2 \times 4.7\,\%$ of the induced signal is lost and induced on adjacent strips. If one uses the values and calculates the redistribution of the signals on all strips, the effect due to cross talk will be obtained.

As one can see in the picture, the effects change the trend of the function from almost a step function to a function that resembles error function. Further, it's evident that if the charge is generated in the middle, i.e. the relative interstrip position is 0.5, the collected charge will be evenly divided between the two strips. In addition, if the charge is generated in interval from 0.4 to 0.5, resp. 0.5 to 0.6, then one would expect that the charge will be almost collected only by one strip, but in reality the charge is again divided between the two strips in ratio given exactly by the η function. Finally, it's obvious that the cross talk effect results in the redistribution of the charge to the neighbouring strips and thus increases the number of strips that will collect a certain amount of the deposited charge. In current parlance, we say that the effect increases the cluster size.

The charge sharing effect can be even seen, if the particle is incident on the detector at zero angle exactly at the center of a strip. In such a configuration (without cross talk effect) the current signals for 180 Gev/c pions crossing the detector have been simulated (10 000 events). The results are shown in fig. 3.7. The black line represents the current on the central strip,

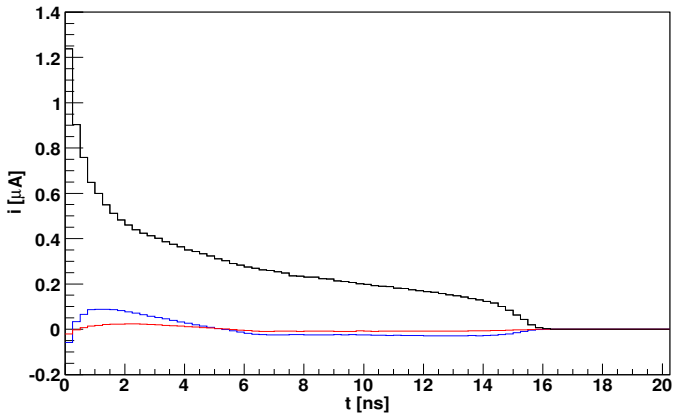

Fig. 3.7: Simulated response of the detector to 180 GeV/c π^- passing the detector at zero angle and in the middle of a strip. Black line corresponds to the current on the central strip, blue line on the left strip and red line on the second strip on the left side.

the blue line on the left strip and the red line on the second strip on the left side. The result can be easily understood if one looks at the weighting potential (fig. 3.4) and the relation (3.6). Let us, for instance, take the left strip and imagine the weighting potential corresponding to the left strip. Even though the weighting potential is small at the central strip region, it causes that a nonzero current will flow on the left electrode, but in total the collected charge will be almost zero.

For the central strip the total signal has been expressed as the sum of a current induced by moving electrons and a current induced by moving holes, see fig. 3.8. Since the electrons have a bigger mobility than the holes, we

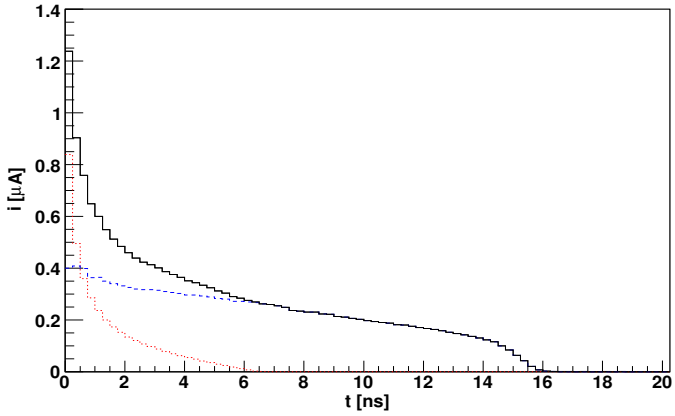

Fig. 3.8: The signal on the central strip (black line) as a sum of a signal due to electrons (dotted red line) and a signal due to holes (dashed blue line).

can naturally expect that the electrons will form a fast component, whereas the holes a slow component and thus will mainly contribute to the signal obtained. If we compare the maximal values of drift time calculated in section 2.7 and summarized in tab. 2.3 with the simulated data, we can say that the results correspond well to each other and the simple approach used for calculation can be taken as adequate for estimation of detector response when simulating particle incident on the strip.

4 SCT Beam Tests Simulations

In 1999–2004, the prototypes of SCT modules were systematically tested in the H8 beam line of the Super Proton Synchrotron (SPS) at CERN. In the beam tests the response of the modules to secondary particles, 180 GeV/c pions with a small fraction of muons, was measured. The main purpose of the tests was to study the dependence of tracking performance of individual modules on a series of external parameters: detector bias voltage, discriminator threshold, angle of incident particles, the interstrip position where the particle crosses the detector volume, magnetic field, etc. The results of these measurements have been used to verify the reliability of created simulations. Simultaneously, based on the comparison of simulations with the real data, we have been able to explain an influence of individual physical effects such as: diffusion, weighting field effect, cross talk and δ-electrons on the response of the detectors. In this chapter, we will focus on simulation performance, explain all the physical effects that are included in the simulation and discuss in more detail the beam test and simulation results. In order to outline the conditions under which the data were taken we will first briefly overview the experimental setup.

The information about the beam tests, including the experimental results that have been used in this chapter, can be found in CERN internal notes [5], [6] and in officially published beam tests results [8]. The experimental setup, the individual tests and the data analysis are well described in [26].

4.1 Test Beam Setup

A typical arrangement of SCT modules in H8 beam line during the beam test in August 2002 is illustrated in fig. 4.1. It consists of two scintillator detectors, 4 beam telescopes and a chamber containing the modules under test. All the system is mounted on a granite table sitting on a trolley that enables the setup to be inserted into a magnetic field of 1.56 T created by the superconducting Morpurgo magnet. The magnetic field is orientated vertically downwards, i.e. for the barrel modules the field is parallel to the strips.

The two scintillators, read out by photomultiplier tubes, detect the pas-

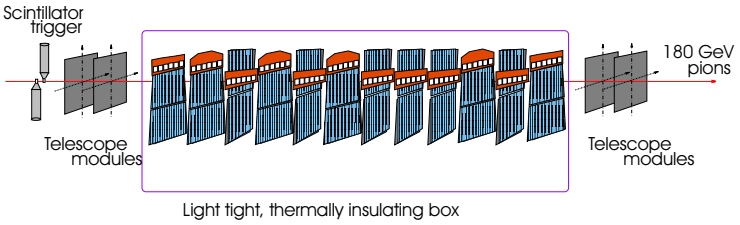

Fig. 4.1: Arrangement of SCT modules in the beam line H8 during the August 2002 beam tests.

sage of beam particles and serve as a trigger for the read-out system. Typical acceptance of scintillator detectors is $2 \times 2\,\mathrm{cm}^2$. It is comparable in size to the acceptance of the beam telescopes and large enough to register the typical beam spots. The two sets of 2 telescopes are used for alignment of the whole system and for reconstruction of the trajectories of incoming particles. Each telescope is composed of two mutually perpendicular wafers with a strip pitch of $50\,\mu$m. The spatial resolution obtained by telescopes is below $5\,\mu$m.

The devices under test are held in a light-tight thermally insulated chamber that is flushed with cold nitrogen gas to ensure a dry atmosphere. Each of the modules is contained in its own aluminium test box to which it is thermally coupled through the designed cooling contacts. As a cooling medium the mixture of water and ethanol is used. The temperature on a hybrid is continuously measured, using a thermistor at the edge of the hybrid. It ranges between -5 and $5\,^{\circ}$C.

4.2 Simulations

In order to validate the simulation software described in previous chapter, the simulation of a single Hamamatsu barrel module under beam test conditions has been performed. The barrel module has been chosen due to simple geometry and a constant strip pitch of $80\,\mu$m. (The parameters of the detector are summarized in table 2.3, the Geant 3 geometry is defined in section 3.2.) The temperature on the wafer has been set to $T = 300\,\mathrm{K}$, the bias voltage to $150\,\mathrm{V}$. (The field maps are the same as shown in previous chapter.)

In the simulation two different approaches have been realized. The first has been used to show the response of the detector to $180\,\mathrm{GeV/c}$ pions that deposit their energy uniformly along the track, but without δ-electrons. The latter has been used to demonstrate the strength of δ-electrons. It sim-

ulates 180 GeV/c pions that cross the detector and generate the δ-rays along the path. (Detailed description of the two alternatives is given in section 3.2.)

In order to emphasize all the facts that had to be taken into account when simulating and analysing the simulated data, let us here give a brief overview of them. We will describe the physical mechanisms of charge collection, the effects connected with the binary read-out system of the detector and uncertainties of position measurements and charge measurements related to the multiple scattering, telescopes resolution and detector and front end electronics noise:

diffusion and weighting field – Particles incident on the detector plane in a central area between two strips (interstrip position ≈ 0.4 – 0.6) generate the e-h pairs exactly in the region where the collection of the charge will be strongly influenced by the charge sharing effect and the random character of diffusion. The electrons and holes, divided between the strips in a ratio given by the η function (see section 3.2), will drift to more than one strip and thus substantially increase the so-called cluster size.

cross talk – The capacitive coupling of the strips, caused by the interstrip capacitance, leads to the induction of a signal on the neighbouring strips. This effect increases the number of strips collecting the charge. In section 3.3 it has been shown that approximately 91 % of the collected charge will be loaded by the electronics and the rest 2×4.7 % will be symmetrically induced on adjacent strips. In the analysis only the capacitive coupling between the strips that are directly neighbouring has been taken into account.

δ-electrons – In a small fraction of collisions between an incident particle and an electron bound in the matter large momentum transfers take place and high energy electrons ($\sim$ tens or hundreds of keV) will be produced. It's evident that such an electron ionizing the medium along its path can increase the number of strips collecting the generated charge, i.e. will increase the cluster size.

ENC – The total noise of the module and the front end electronics substantially influences the collected charge from the strip. In order to simulate this effect the collected charge has been smeared by the Gaussian distribution with $\sigma \approx 1500$ e.

telescope resolution – The precision of reconstructed track position is determined by the accuracy of telescopes measurements $\approx 5\,\mu$m. This

uncertainty of interstrip position has been simulated by adding a random number, distributed according to the Gaussian distr. with sigma $5\,\mu$m, to the known position.

multiple scattering – Another effect that influences the precision of track position is the multiple scattering of beam particles in the detectors and additional material. The distribution of deviations from the real tracks given by the telescopes can be estimated as Gaussian with sigma $6\,\mu$m.

discriminator threshold – The detector modules, namely the electronics, were operating during the beam tests on a threshold 1 fC set on discriminator. This optimal value was set to reduce considerably the noise and simultaneously to hold the efficiency of the detector higher than 99 %. The detector is considered efficient if a binary cluster centre detected by a module is located within $150\,\mu$m from the interpolated telescope track position.

4.2.1 Median Charge

In order to reconstruct the full analogue signal in the binary read-out scheme, it is necessary to perform the discriminator threshold scan for each strip. The obtained result: efficiency as a function of the threshold represents the integrated charge distribution, the so-called "s-curve". The specific shape of the curve can be described as a convolution of "Landau" distribution of deposited charge, Gaussian distribution of noise, the effect of charge sharing and the fact that the system has a binary read-out. In order to outline why these effects have such a substantial influence on the data, we will mention the way how the s-curve was measured: the binary results were taken into account from two neighbouring strips, independently on the position of the track between them. If at least one of the signals was above the threshold, the statistics of s-curve for the given threshold was increased of one, if not no signal was registered.

Even though the median charge can be measured as the charge corresponding to the threshold where 50 % efficiency is obtained, in practice, the threshold was expressed in equivalent charge and the median was obtained directly from a fit with a skewed error function (see [8]):

$$\varepsilon = \varepsilon_{max} f\left(x\left[1 + 0.6\frac{e^{-\xi x} - e^{\xi x}}{e^{-\xi x} + e^{\xi x}}\right]\right) \tag{4.1}$$

where f represents the complementary error function, ξ the skew, ε_{max}

the maximum efficiency and $x = (q_{\text{threshold}} - \mu)/\sqrt{2}\sigma$ the variable. The median charge is in the relation denoted as μ and the width as σ.

The average median charge of significant number of unirradiated barrel and outer end-cap modules was from the beam tests evaluated as (3.5±0.1) fC at a bias voltage of 300 V. When we compare the result with the simulations of 10 000 events (see fig. 4.2), we will get a similar value (3.41±0.04) fC, where

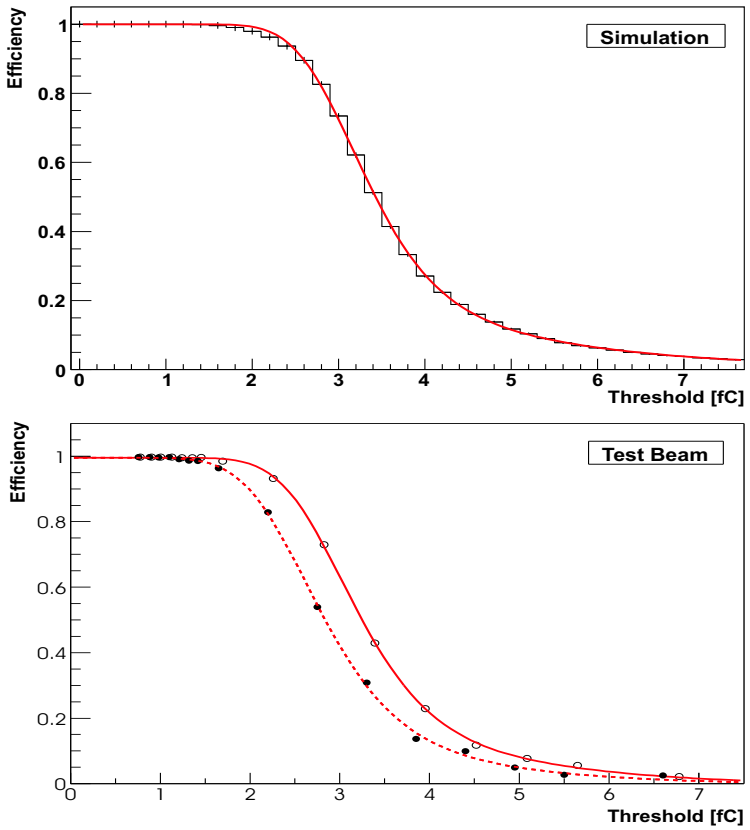

Fig. 4.2: Typical efficiency versus threshold, "s-curve". The simulation is shown at the top, the beam tests result at the bottom. The solid red line corresponds to a nonirradiated module, the dashed red line to an irradiated module.

the error has been estimated from the difference between the real deposited charge in the detector and the total simulated collected charge on the strips. (In simulation the value of collected charge fluctuates around the average by 1% ≈ 0.04 fC. It is related to the optimal choice of simulation step.)

In order to illustrate how particular physical effects influence the median charge, the simulations have been performed in the following way. The individual effects: diffusion together with weighting field, cross talk and δ-

electrons have been added to the simulations one by one. First, the simulation of 180 GeV/c pions incident on the center of a strip has been made. Such a configuration has been chosen due to strong suppression of charge sharing effect. The obtained value (3.94 ± 0.05) fC is in perfect agreement with the value of deposited charge (3.91 ± 0.02) fC that has been calculated from the mean energy loss (89.0 ± 0.5) keV (see fig. 3.5), using the average energy of 3.65 eV needed for production of one e-h pair. Further, the pions have been simulated crossing the detector randomly between two strips, when the effects of diffusion and weighting field become crucial for the charge collection. The result is equal to (3.81 ± 0.05) fC, so that approximately 0.10 – 0.13 fC of deposited charge can be regarded as lost due to charge sharing. When the cross talk has been added, we have obtained (3.43 ± 0.05) fC that is practically equal to the experimental value. From the simulations it's obvious that almost all the difference between the deposited charge and the measured charge is given by the effect of interstrip capacitance. The contribution of δ-electrons to the loss of deposited charge is rather negligible. The median obtained by simulations with δ-rays together with other effects has been (3.41 ± 0.04) fC.

4.2.2 Incidence Angle

In the beam tests the measurements were performed at various angles, both in the plane perpendicular to the strips ($R\Phi$ plane) and the plane parallel to the strips. The simulation has been reproduced for the first situation and the dependence of median collected charge on the angle of incident pions has been studied.

In this type of measurements two mutually opposite effects exist. The first effect is given by the geometry. Particle incident at a certain angle has a longer path with respect to the perpendicular incidence and thus the deposited charge increases, approximately as $1/\cos(\alpha)$. On the other hand the amount of collected charge on a strip is strongly influenced by the charge sharing effect. The charge is distributed among more strips than in case of perpendicular incidence and the median collected charge can decrease.

The beam test results indicate that for the geometry of SCT modules the charge sharing effect prevails and becomes more substantial than the first effect. The simulations confirm this result. The comparison of simulations with measurements is depicted in fig. 4.3. The simulations have been performed for $0\,^\circ$, $2.5\,^\circ$, $5\,^\circ$, $10\,^\circ$, $15\,^\circ$ and symmetrically in negative values. The results have been further fit with a smooth curve. The measurements were performed in non-equidistant values of angle.

In the simulations the influence of individual effects: diffusion and weight-

ing field effect, the two preceding effects together with cross talk and all the effects together with δ-electrons have been studied. From the comparison it's obvious that the results are in a good agreement with experimental values. Moreover, it can be seen that the influence of δ-rays becomes important for the angles greater than $5\,^{\circ}$.

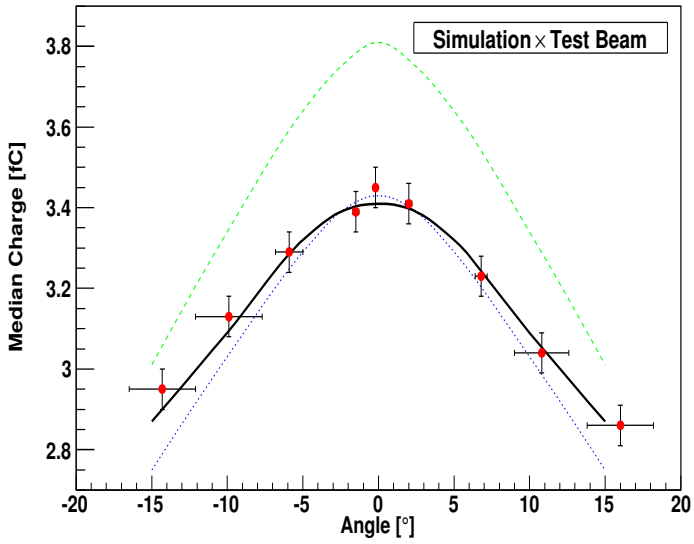

Fig. 4.3: Median collected charge versus incidence angle in the $R\Phi$ plane. The simulation is depicted in three variants: without the cross talk effect and without δ-electrons (green dashed line), with cross talk but without δ-rays (blue dotted line) and with all effects together (black solid line). The curves have been obtained from a fit of simulated data with smooth curves. The measurement results are shown as red markers and refer to the response of a barrel module measured in 2001.

Another task has been the measurement of a cluster size versus the incidence angle. The cluster size is defined as a number of strips that collect the charge when a particle crosses the detector volume, randomly between two strips, and simultaneously the signals obtained will be above the set threshold 1 fC. At the beginning of this section a few mechanisms, that can considerably influence the value of cluster size, have been summarized. The most important are: the charge sharing effect, cross talk and δ-electrons. From the simulations (see figure 4.4) it is evident that even though the δ-rays have high energy enough to influence the cluster size, the number of them is very low and they don't substantially contribute to the change of cluster

size. (From relation (2.47), using $T_{cut} = 140\,\mathrm{keV}$, the number of δ-electrons produced in $285\,\mu\mathrm{m}$ thick silicon bulk can be estimated as 0.035. The energy cut has been chosen based on the simulated distribution, see fig. 3.5.)

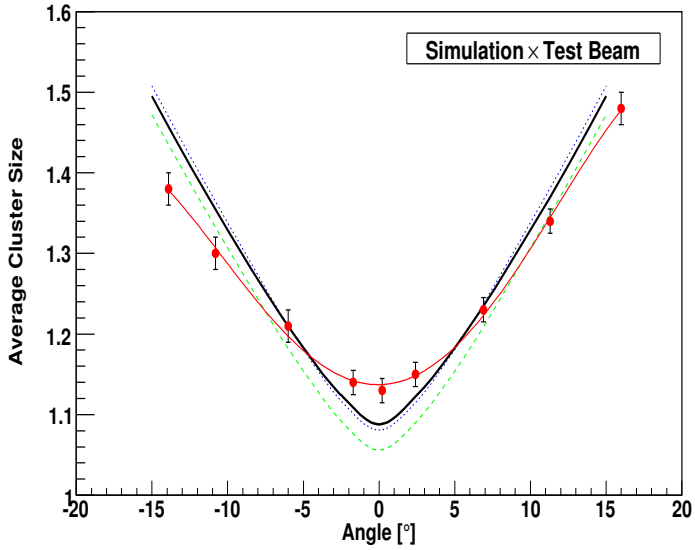

Fig. 4.4: Cluster size versus incidence angle for non-irradiated modules at threshold 1 fC. The simulation is shown in three alternatives: without the cross talk effect and without δ-electrons (green dashed line), with cross talk but without δ-rays (blue dotted line) and with all effects together (black solid line). The curves have been obtained from a fit of simulated data. The filled red markers that have been fit with a polynom represent the measurements.

The trend of angular dependence of cluster size is apparently in a good agreement with the measurements, but the values for angles around $0\,^\circ$ are underestimated and the values for angles higher than $10\,^\circ$ are overestimated. The values differ by $\sim 4\,\%$. The discrepancy could be explained by a few effects. One of them could be the effect of interstrip capacitance between not directly neighbouring strips that is missing in the simulation. From preceding comparisons of real data with the simulations it's evident that the cross talk has an important influence on the obtained results. Thus, the mentioned contribution of secondary cross talk that has not been included in the simulation could improve the results.

4.2.3 Interstrip Position

The measurements and the simulations have been also concentrated on detector performance with respect to the interstrip position, where a particle crosses the detector volume, and different thresholds set on a discriminator. The efficiency measurements represent a good test of SCT detector performance. They demonstrate how the detector is sensitive to a particle with respect to the position of incidence and the set discriminator threshold. The detector has been designed to have efficiency higher than 99 % at the nominal value 1 fC set on discriminator. This fact is connected with the physics we want to reconstruct. Still one more remark, the detector wafer is considered efficient if a binary cluster center is located inside a region within 150 μm from the reconstructed track. The measurements together with simulations are shown for different thresholds in figure 4.5.

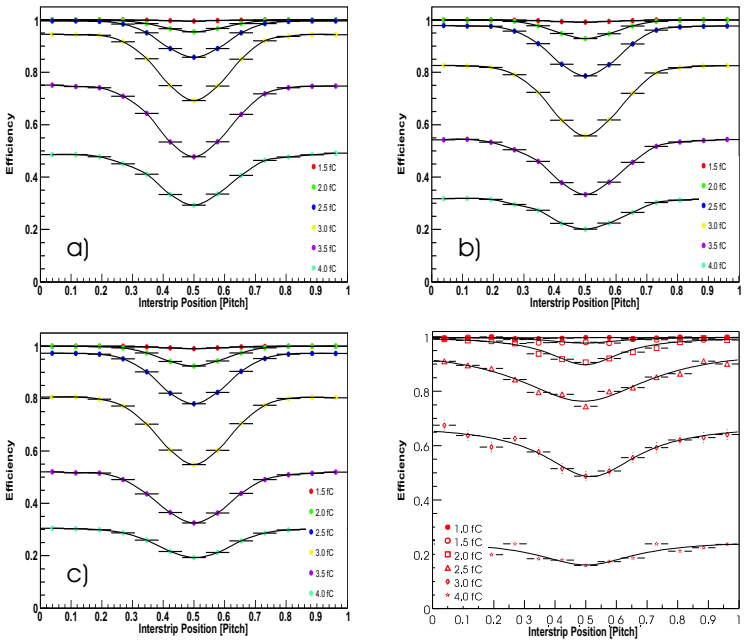

Fig. 4.5: Efficiency as a function of the inter-strip position of the incident particle for a nonirradiated barrel module. The graph at the top on the left (a) has been simulated without cross talk and δ-electrons, the graph at the top on the right (b) has been simulated with cross talk but without δ-rays and the graph at the bottom on the left (c) has been simulated with all effects together. The results of measurements are shown at the bottom on the right. Different color of markers, resp. the shape of markers, correspond to different thresholds set on a discriminator.

The trend of the curves and particularly the decrease of efficiency in the central area between the strips is in a good agreement with the experimental results. The small discrepancy (The simulated efficiency is a little higher than the measured one.) could be again explained by the contribution of secondary cross talk that is missing in the simulation.

In order to show how the cluster size is dependent on the interstrip position, we have simulated a particle incident uniformly between two strips at angle 0 ° and compared that to experimental results, see figure 4.6. The simulation has been performed at a threshold 1 fC.

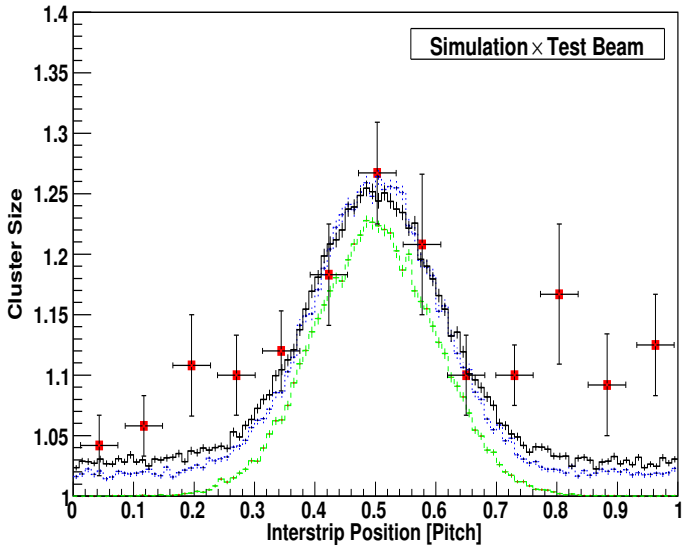

Fig. 4.6: Cluster size as a function of the interstrip position of the incident particle for a nonirradiated barrel module. The simulated histogram are shown in three variants: without the cross talk effect and without δ-electrons (green dashed line), with cross talk but without δ-rays (blue dotted line) and with all effects together (black solid line). The red markers represent the test beam measurements.

The trends of both the simulations and the measurements are very similar. Particularly, the increase of cluster size due to charge sharing effect and cross talk can be seen in the picture. From the comparison of individual simulations (The contribution of particular effects is important.) it's evident that the results are almost the same. No important effect of δ-electrons can be seen, only the cross talk slightly increases the cluster size at small and high interstrip positions.

4.2.4 Summary

In this section the validity of the simulation program has been verified. The results have been compared to the experimental data for different types of measurements and a good agreement between the simulations and the results have been found. Moreover, based on the simulations it has been explained how the basic physical phenomena affect the measured results. When we have compared the results with the data, it has been evident that all the mentioned effects: diffusion, weighting field effect, cross talk and δ-electrons must be taken into account. The effect of charge sharing together with cross talk have played an important role in all results, the δ-rays only in the measurements of median collected charge versus incidence angle and slightly in efficiency measurements.

The comparison of the median collected charge measurements with the simulations has confirmed that the total charge loss $\sim 0.4\,\mathrm{fC}$ due to the physical mechanisms mentioned above explains the discrepancy between the observed median charge ($3.5\,\mathrm{fC}$) and the expected value ($3.9\,\mathrm{fC}$). Further, the simulation has confirmed that the response of the detector is strongly dependent on the set threshold on a discriminator (see efficiency graphs) and that the efficiency at threshold $1\,\mathrm{fC}$ corresponds roughly to $100\,\%$. Finally, the cluster size has been studied. It has been shown that for small angles the simulated cluster size is underestimated and for the angles higher than 10° is overestimated. As an explanation of this discrepancy the effect of missing secondary cross talk can be proposed.

5 Laser Simulations

In this chapter our approach to the simulations of detector response to a laser beam will be described. First, we will briefly concentrate on the experimental setup and describe the results. Further, our geometrical conception of a laser beam behaviour in a silicon microstrip detector will be presented and at last the simulations based on the model will be compared to the measurements and discussed in more details.

The high precision measurements that are presented here have been performed by P. Kodys in Prague [11]. The details about the laser method as well as the laser tests are well described in [9].

5.1 Experimental Setup

During the laser tests the microstrip detector is held in a light-tight thermally insulated box that can be cooled down in a dry atmosphere to almost $-20\,^{\circ}\mathrm{C}$. As far as the device under test is concerned it is fixed in the box whereas the laser optic is placed on a moving stage. The stage allows the lens to be set with a high accuracy in the space and to light the detector under defined conditions. In our case the stage can move in three mutually perpendicular directions (x, y and z) with a precise step of $1.25\,\mu$m and an accuracy $\approx 0.2\,\mu$m. The rotational motions are also available, in two angles – ϑ and φ. Due to them the high precision angular scans with the step of $0.01\,^{\circ}$ are possible.

The laser pulse from an infrared semiconductor laser ($\lambda = 1060\,\mathrm{nm}$) is generated after a trigger signal from the Data AQuisition electronics (SCT DAQ) is received. The created light is then led through an optical fibre with a lens at the end and is focused on the surface of the detector. The typical distance, at perpendicular incidence of a laser, between the detector and the optic is approximately 12 mm [11]. In order to be able to directly register the signal from the laser, the optical fibre splitter and the light converter (it converts the light into an electric signal) is used. The obtained signal from the converter can be displayed on a screen of an oscilloscope.

After the laser beam hits the detector surface, it is refracted into n-bulk

and then exponentially attenuated in the material. For the measurements the use of an infrared laser of 1060 nm is very interesting since the light penetrates deeply into the silicon material and thus behaves in a more similar way as a MIP. On the other hand if one compares the laser with a particle, a few optical effects, that complicate the situation, have to be taken into account: reflection and refraction of the beam on surfaces of a detector. Particularly, on the aluminium back side and the aluminium strips almost the whole signal is reflected. On the interface between the silicon and the protecting layers, resp. between the silicon and air, a large amount of the signal is lost due to the refraction and the light escapes from the detector volume. The schematic layout of the setup, including the real picture of the apparatus, is depicted in fig. 5.1.

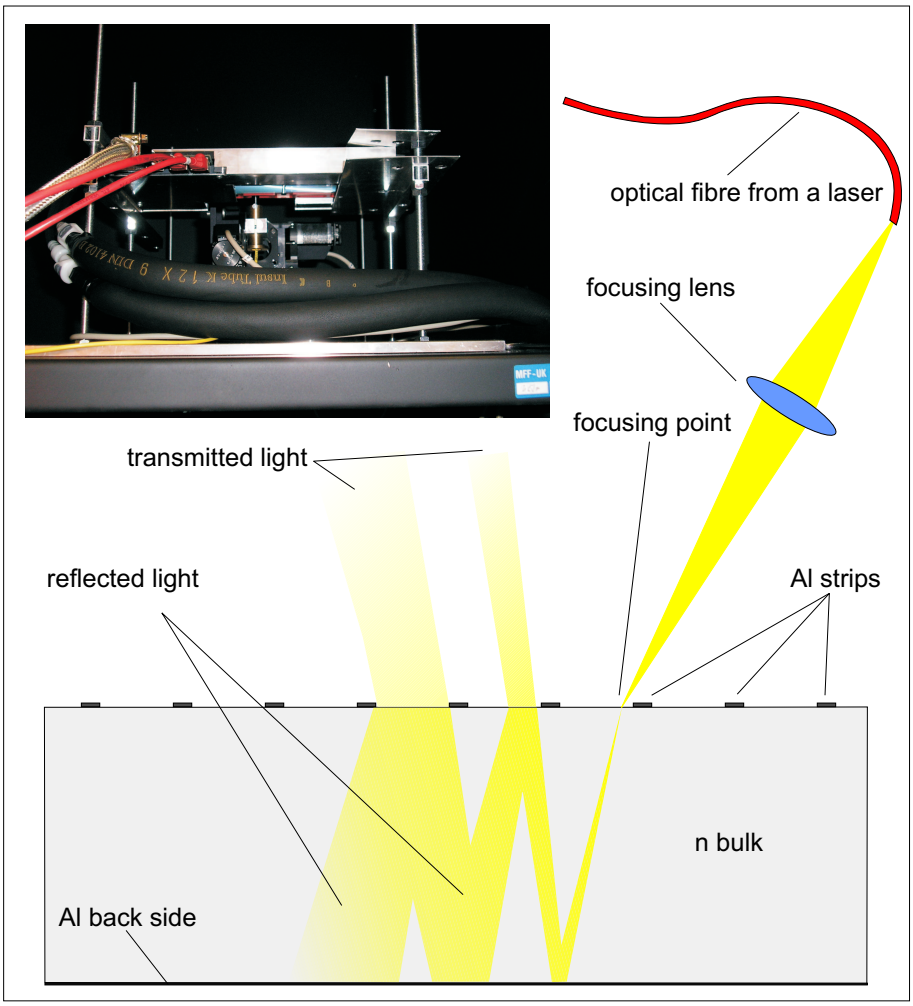

Fig. 5.1: Schematic Picture of a Laser Setup

5.2 Simulations

Due to the fact that the response of the detector simulated in Geant 3 environment can be performed only in a range of particle energies from 10 keV to 10 TeV and the energy of a laser photon (1060 nm) is substantially smaller (1.17 eV), we had to develop our own simulation of e-h pairs generation based on a simple geometrical conception. In order to show why the simple model has been chosen and to show which input parameters are necessary for the description, we will first present the experimental results and then the geometrical model.

5.2.1 Experimental Results

The measurements have been done for both types of detector modules: CiS and Hamamatsu. Moreover, the end-cap modules (the strip pitch is not constant along the detector) have been tested, so that the results are dependent on the laser position. The typical response of a microstrip detector for the laser moving across the strips is depicted in fig. 5.2.

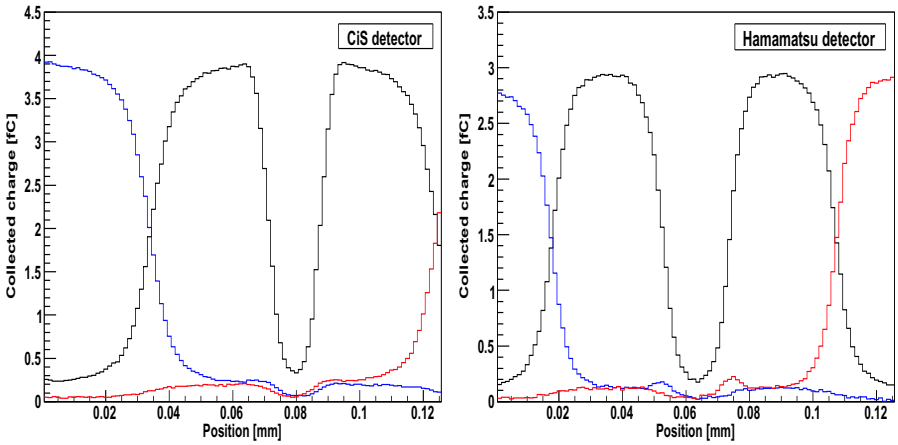

Fig. 5.2: Typical response of a microstrip detector (CiS and Hamamatsu) to a laser beam perpendicularly incident on a detector surface and moving across the strips. The blue line corresponds to a signal on the left strip, the black line on the central strip and the red line on the strip on the right.

As one can see, the two plots differ in the shape of the signal, particularly in the minimum between two peaks (CiS is steeper and sharper). These effects can be explained when we look at the schematic picture of the strip architecture shown in fig. 1.6, especially, on the width of aluminium strips

and the structure of individual layers. The aluminium strip reflects almost all the light incident on the surface and thus only a small fraction of photons will generate e-h pairs inside the detector volume. As a result the measured signal decreases in the area of a strip. (See the signal minima at position 0.08 mm, resp. 0.065 mm.) Further, the complicated structure of the layers can result in the light scattering and thus can make the measured signal smoother for the Hamamatsu detector than for the CiS detector.

Based on the measurements we have been able to characterise the properties of the beam profile and to find out the values of the strip widths. In the analysis the profile of the beam has been supposed to be gaussian and the data on the left side of the signal decrease have been fit with a complementary error function and on the right side with an error function. The fits are shown in fig. 5.3. As one can see, it's obvious that the gaussian distribution

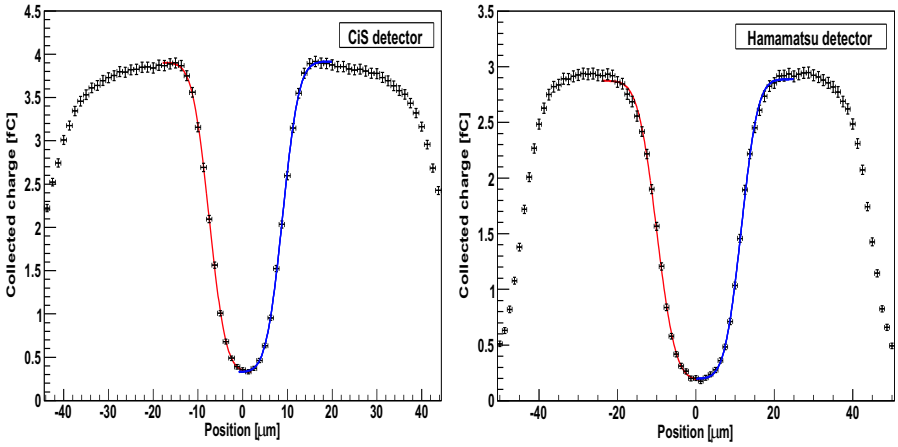

Fig. 5.3: The fit of a signal, in a strip area, with a complementary error function (red line) and with an error function (blue line). In this area the laser is strongly reflected from the outside of aluminium layer. The fit has been performed for both types of detectors (CiS and Hamamatsu).

of the laser intensity well corresponds to the data and the laser profile can be regarded as gaussian with σ obtained from the fit. The limit for the sigma has been from CiS measurements evaluated as $(2.86 \pm 0.07)\,\mu$m and from Hamamatsu measurements as $(3.55 \pm 0.10)\,\mu$m. The different values can be explained by different structure of the protecting layers (see fig. 1.6). For Hamamatsu detector the light scattering probably increases the measured width of a laser and thus the bigger σ has been received. On the other hand, for the CiS detector the structure is simpler and the more realistic value of σ has been obtained.

The distance between the two peaks of signals measured on adjacent strips (see fig. 5.2) gives the pitch of the detector in a place, where the laser has been focused. For both types of detectors the pitch has been evaluated as $(90.0 \pm 0.5)\,\mu$m.

From the medians of the fits, namely from the difference of the values, the width of aluminium layers has been calculated. For CiS detector the value is $(16.1 \pm 0.5)\,\mu$m and for Hamamatsu $(21.6 \pm 0.5)\,\mu$m. If we compare the results to the values specified by producers (CiS detector $\sim 16\,\mu$m, Hamamatsu detector $\sim 22\,\mu$m), we can say that the values (specified and measured) well correspond to each other.

5.2.2 Geometrical Model

Based on the experimental experience the laser has been described by means of geometrical optics, no wave optics effects have been included in the simulation (no interference effects, diffraction effects ...). The basic optical parameters (for 1060 nm light in a silicon material) as well as other parameters of a silicon microstrip detector (different from those summarized in tab. 2.3) are overviewed in table 5.1. These parameters have been used as

Variable	**Value**
Wavelength of a laser beam	1060 nm
Laser energy of a photon	1.17 eV
Refraction index	3.554
Attenuation length	894.2 μm
Absorption coefficient	1.12 mm^{-1}
Temperature	300 K
Detector pitch	90 μm
Width of Al layer (CiS)	16 μm
Width of Al layer (Hamamatsu)	22 μm

Tab. 5.1: The optical parameters (for 1060 nm light) together with other parameteres of a silicon microstrip detector.

an input for the simulations.

The simulation of e-h pairs generation is performed in the following way: The laser beam incident on the surface of a microstrip detector is refracted into the material according to the Snell's law and then exponentially attenuated until the intensity decreases below 3 % of initial value. During the motion the beam is reflected on the edges of the detector. The coefficients of

reflection have been estimated based on the data extrapolation, presented in [9], as 90 % for Al back side and 90 % for Al strips. The reflectivity of the interface between the silicon and air has been calculated as for unpolarised light from the known Fresnel's relations. The value is 32 %. The profile of the beam has been in direction perpendicular to the motion described as gaussian with $\sigma = 2.8\,\mu$m. Moreover, due to the optics the beam has been regarded as uniformly divergent in the direction of motion. The parameter of divergency can be found from the simulations. Finally, if a fraction of the laser beam is incident on the surface of a strip from the outside, the photons will be reflected and no e-h pairs will be generated in the detector.

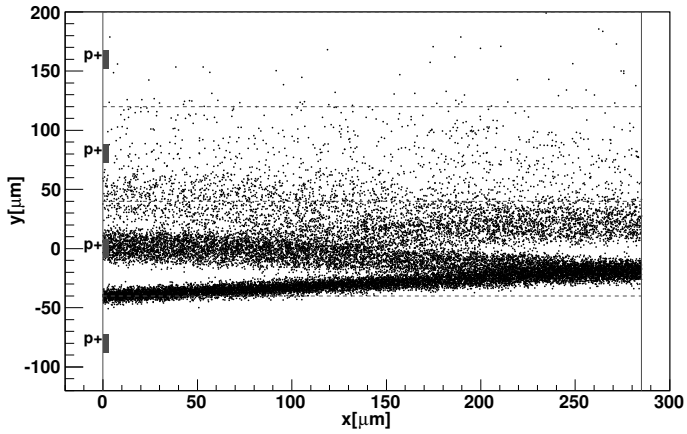

Fig. 5.4: The generation of e-h pairs by a laser beam incident on the detector at angle 15 °. The p^+ layers represent the material doping, the dashed lines the borders of individual elementary cells and the solid lines the edges of the detector.

In this model we have supposed that each photon generates exactly one e-h pair. The total charge of simulated pairs has been equivalent to a charge of MIP, i.e. to 4 fC. Due to the fact that in an experiment we don't know the deposited charge by the laser, the maximum of simulated signal has been scaled to the maximal value obtained in the measurements. An example of e-h pairs generated in the detector by the laser incident at angle 15 °, i.e. the inner angle is equal to 4.17 °, is shown in fig. 5.4. From the picture the divergency of the beam can be easily seen.

5.2.3 Results

In order to reproduce the experimental results, we have simulated the response of both CiS and Hamamatsu detectors. In the simulations the laser beam has been incident randomly between four strips on the surface of the wafer and the angle has been set to a zero value. Due to the fact that the strip pitch of 90 μm has been different from the pitch of barrel detectors, the electric field and the weighting field had to be again evaluated in MAXWELL 2D package [1] and converted into a histogram file. The obtained results of electric field as well as the weighting field are very similar to those presented in chapter 3. In the experiment the testing box has not been cooled down, so that the temperature of a silicon wafer has been set to $T = 300\,\mathrm{K}$ in the simulations. Finally, the results have been compared to the measurements and the divergency parameter has been tuned. For both types of detectors the response is depicted in following figures: for CiS detector in fig. 5.5, for Hamamatsu detector in fig. 5.6.

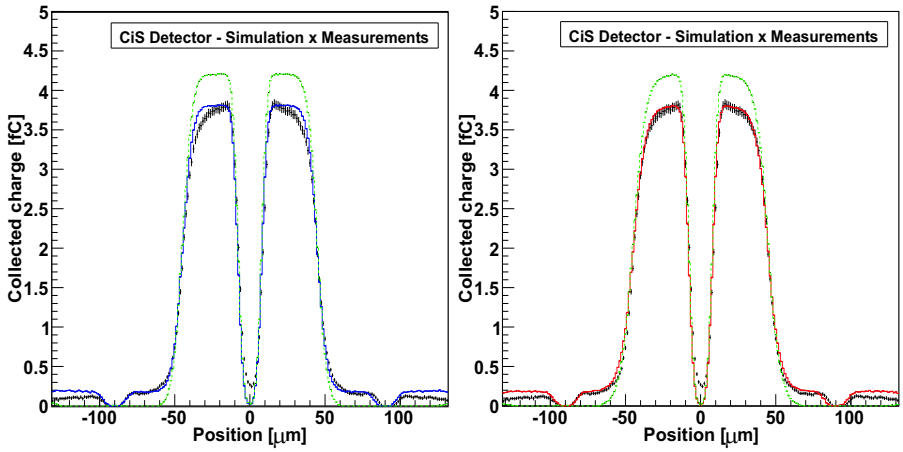

Fig. 5.5: The response of a CiS detector to a laser beam incident perpendicularly on the surface of the wafer. The left picture demostrates the simulation with a divergency of the beam $\pm 0.50\,^\circ$ (blue solid line) and the right picture the simulation with a divergency $\pm 1.25\,^\circ$ (red solid line). The green dashed line represents the simulation without cross talk effect and the black line the measurements.

In both figures the effect of cross talk is visible. Moreover, the figures are depicted with the smallest simulated divergency $\pm 0.50\,^\circ$ and the biggest one $\pm 1.25\,^\circ$. (The simulation has been made for different divergencies: $\pm 0.50\,^\circ$, $\pm 0.75\,^\circ$, $\pm 1.00\,^\circ$ and $\pm 1.25\,^\circ$.) The response of the detector without the cross talk effect is shown as a green dashed line, the full simulation with a diver-

gency of the beam $\pm 0.50\,^{\circ}$ as a blue solid line and with a divergency of the beam $\pm 1.25\,^{\circ}$ as a red solid line.

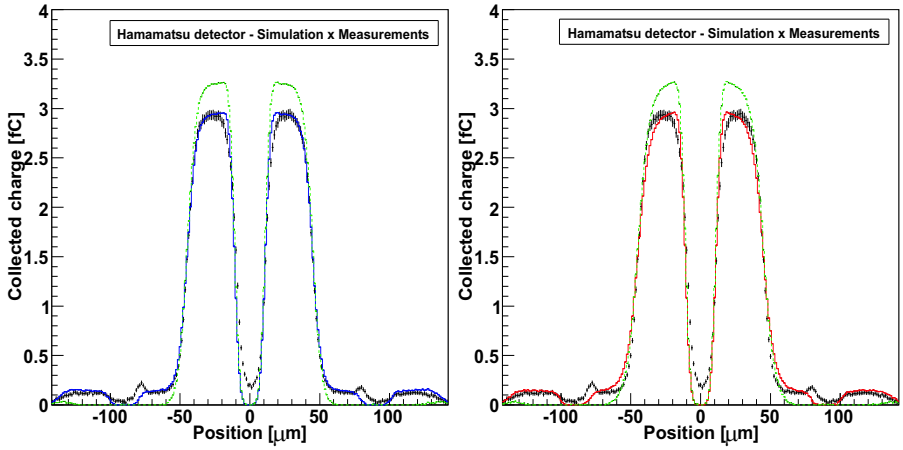

Fig. 5.6: The response of a Hamamatsu detector to a laser beam incident perpendicularly on the surface of the wafer. The left picture demostrates the simulation with a divergency of the beam $\pm 0.50\,^{\circ}$ (blue solid line) and the right picture the simulation with a divergency $\pm 1.25\,^{\circ}$ (red solid line). The green dashed line corresponds to the simulation without cross talk effect and the black line to the measurements.

Let us first comment the CiS detector response. As can be easily seen from the picture, the divergency parameter that well corresponds to the data is $\pm 1.25\,^{\circ}$. From the comparison it's evident that there are a few discrepancies between the simulation and the measurements.

The first one is that the signal registered in the middle of the strip doesn't decrease to a zero value. Based on the simulation a new scan has been made, not on the strip, but on the bond pad (It has a few advantages, the pad is wider and there are no protecting layers there.) and the result is following: The signal has decreased to almost zero value. It means that the protecting layers can be regarded as waveguides that enable to a fraction of light to get into the n-bulk even though the laser is incident exactly at the aluminium strip. (Approximately 0.2 fC, i.e. 5 % of deposited charge, can be explained in this way.) And due to the fact that the signal hasn't decreased totally to the zero value, the laser is not exactly gaussian, but a small "halo" effect (approximately 1 % of deposited charge) can be seen there.

The second discrepancy can be seen in the regions around the left and right strip. As we know, the signal obtained there is only given by the cross talk effect. Unfortunately, the cross talk has been calculated from the capacitances known for Hamamatsu detector since for CiS detector they are not

known. It's possible that if we simulate the response with the appropriate values, we will get the correct results.

The response of Hamamatsu detector (The divergency parameter that well corresponds to the data is $\pm 0.50\,^{\circ}$.) is more complicated. The discrepancy in the region of a strip can be again explained by the effect discussed above. But another differencies exist there. If one looks at the top of two peaks, the simulated curve deviates from the experimental one by $\approx 0.1 fC$ and the measured signal is lower than in the simulations. On the other hand exactly in the same regions at adjacent strips the increase of a signal can be seen. (The amount of decreased and increased signal is approximately the same.) This could be explained in following way: We suppose that the layers can behave as waveguides, so that it can be probable that in the region of a strip the light signal will get into the "waveguide" and at the other end will be diverted back to the silicon.

The last problem is the difference between the divergencies of laser in CiS and Hamamatsu detector. Naturally, one expects that the characteristics of the beam should be the same. In case of CiS detector the correct cross talk could lower the divergency parameter that fits the data. Moreover, for both detectors the parameters of reflectivities should be properly known, mainly for the interface between the silicon material and air. Finally, the refractive indicis can be different for both types of detectors. All these parameters together could improve the agreement of both detectors. From experiment the expected value of divergency is around $\pm 1\,^{\circ}$.

Still one more comment is in order here. The data presented in this section have been measured two weeks before completion of this work and suffer from a minor error given by the nonlinear relation between the electronics response and the real collected charge. (For simplicity, a linear relation has been supposed in the data analysis.) The corrections are mainly important in the region of low deposited charges (up to 0.4 fC) and can change the data in a range of ± 0.1 fC. More sophisticated analysis is planned to be done in the future.

5.3 Summary

In this chapter we have studied the specific response of a microstrip detector to a laser beam using Monte Carlo simulations. Due to the fact that the Geant 3 framework is not suitable for the simulation of e-h pairs generation by the laser, we had to develop own geometrical model and to describe in a simple way the physics lying behind that. The parameters that characterize the model have been defined based on the experimental experience and

extracted from the measurements. The important detector parameters are: the aluminium strip width, the pitch, detector thickness, the bias voltage, the aluminium reflectivity and the reflectivity of the interface between the silicon and the individual layers covering the detector; the laser characteristics are: the gaussian sigma, the divergency of the beam and the attenuation coefficient. The most of them have been well known, but the width of metallic layer and the sigma of the beam had to be obtained from the measurements. For CiS detector the Al layer is $(16.1 \pm 0.5)\,\mu$m, for Hamamatsu detector $(21.6 \pm 0.5)\,\mu$m. The obtained gaussian sigma is $2.8\,\mu$m.

The simulations for both types of detectors (CiS and Hamamatsu) together with the measurements have been compared and a few differences have been found. In order to explain some of the discrepancies a new scan on the bond pad (not on the strip) has been done and some of the effects could be explained. The most important result is that the light can generate the e-h pairs on the strip even though the laser illuminates the aluminium layer (Naturally, one expects that the laser will be reflected on a metallic strip). As a probable explanation of this effect a following idea has been suggested: The protecting layers can behave as a waveguide and thus can lead the light from the metallic layer into the detector.

Conclusion

At the beginning of September 2005 I was faced with a basic problem to develop a simulation tool, with its help we would be able to explain the specific response of a silicon microstrip detector (SCT ATLAS) to a laser signal, to interpret correctly the measured data and to suggest new physically interesting measurements. Simultaneously, it was desirable to study with the help of developed simulation the influence of individual physical processes leading to the generation and propagation of e-h pairs in a silicon material and to understand properly the response of the detector.

For this purpose a full two dimensional Monte Carlo simulation of charge collection in a microstrip detector has been developed (based on conception of F. Loparco and N. Mazziotta [13]) and implemented into Geant 3 software framework, with the so-called PAI model (PhotoAbsorption Ionization model) set for the simulation of energy loss distribution as default. The Landau distribution (automatically used in Geant 3) has been compared together with PAI model to the experimental measurements (taken from [7]) and an interesting result has been found. For a thin silicon material and high energetic particles the energy loss distribution simulated using Landau formalism doesn't correspond to the reality and thus a special model (PAI) taking into account the atomic structure must be used.

In order to verify the validity and reliability of the whole simulation software, the simulated data have been compared to the experimental results, obtained from the beam tests measured in CERN in 1999-2004, and a good agreement has been found. Particularly, we have studied how the individual physical effects: charge sharing effect, diffusion, δ-electrons and the cross talk effect influence the obtained results for a Hamamatsu detector. In the simulations two different approaches have been used, the first simulating the response to 180 GeV/c pions uniformly ionizing the material along its path, the second corresponding to a full simulation with δ-electrons. The study of simulations together with measurements has shown that the most substantial influence on the results can be attributed to a cross talk. The influence of charge sharing effect together with diffusion is mainly important in the central region between two strips (i.e. for interstrip positions [in pitch] between 0.4 to 0.6), whereas the effect of δ-electrons is mostly negligible. They slightly

contribute only for high incidence angles to the results of median collected charge measurements.

In addition to that, with the help of simulation the difference between the expected deposited charge ($\sim 3,9\,\mathrm{fC}$) and the real collected charge ($\sim 3.5\,\mathrm{fC}$) has been explained. We have found that the loss of approximately $0.1\,\mathrm{fC}$ can be explained by the charge sharing effect together with diffusion and approximately $0.4\,\mathrm{fC}$ can be explained by the cross talk. The δ-electrons don't substantially contribute to the difference between the expected and measured value.

Due to the fact that the Geant 3 environment is not suitable for the description of a laser behaviour in a silicon microstrip detector, a simple geometrical model based on general principles of geometrical optics has been developed and the response of both different types of detectors (CiS and Hamamatsu) to 1060 nm laser has been simulated.

For both types of detectors the trend of simulated response has well corresponded to the response obtained from the experiment, but a few differences have been found. The differences have pointed out that the simple approach of a gaussian beam (with a defined divergency and reflecting on surfaces of detector) doesn't exactly describe the observed response and new effects exist there. These discrepancies have been explained after a new measurement on a bond pad without any protecting layers has been made and compared with the simulations. The important result is that the light can generate the e-h pairs on the strip even though the laser illuminates the aluminium layer. As a probable explanation of this effect a following idea has been suggested: The protecting layers can behave as a waveguide and thus can lead the light from the metallic layer into the detector.

Appendix A

The appendix provides the basic information about the developed simulation software and is particularly intended as a tutorial for people who may be interested in the simulations. The simulation package is designed for use in the Linux operating system and is available on the web page [20]. The software consists of the simulation source codes, the executable files, the shell scripts, the data files and the parameter files controlling the simulation input parameters. The files have been compiled using the GNU Fortran 77 compiler `g77` and CERN program libraries: `cernlib` and `geant321` (see [22], [23]). (The "makefile" is denoted as `g77l` and can be found in a directory `simulation/bin`.) For simplicity and for easy application of the simulation, each program has the same directory structure and contains the same types of files:

- `./datafiles` - a directory that contains the data files used as an input files for the program, resp. simulation. Let us summarize here the two most important of them: the histogram file containing the field maps of a detector (`elmagfld.his`) and the file that contains the energy loss distribution in a silicon microstrip detector (`landdistr.his`). Moreover, the so-called parameter file `*.par` can be found here. The file specifies the parameters of the program, resp. the simulation, such as: input file, output file, number of events to be simulated, parameters of a detector, parameters of the laser beam, etc.

- `./macros` - a directory that contains the source codes of the program, resp. the simulation, the executable files and the `root` macros needed for visualisation of particular results.

- `./simulation` - the shell script that serves to execute the program. It takes as an input the parameter file and redirects it to the executable file. After the simulation finishes, it controls the operations to be done, for instance the conversion of the output file from the `hbook` format [24] to the `root` format [25], using `h2root` routine.

- `./.` - the output files (`*.hbook`, `*.root`) are saved here.

A total of five programs are presented here (The source codes are well commented so that only a brief description of the programs themselves will be given here.):

- `simulation/field` - it serves as a conversion routine. The main purpose is to convert the exported data of electromagnetic field and the weighting field from the MAXWELL 2D simulation tool [1] to the `hbook` format. The name of the output histogram file is specified in a parameter file `dat2hbook.par`. The histogram file must be copied to the directory `./datafiles` of a selected simulation, after the conversion finishes.

- `simulation/landau` - it generates the energy loss distribution of an incident particle in a detector and saves it in the `hbook` format. In the parameter file (`landdistr.par`), one can define a particle type, its absolute value of laboraty z-axis momentum (in GeV/c) and the number of simulated events. In order to change the detector geometry, one has to change the source code in a file `landdistr.f`. The output file `landdistr.his` is necessary as an input file for the simulation program `simulation/partntuple`.

- `simulation/laserntuple` - the simulation of a detector response to the laser beam. The simulation output can be influenced by the change of the parameter file `laserprop.par`. One can change the width of Al layer (in μm), the depth of p^+ layer (in μm), equivalent charge (in fC) generated by the laser beam, attenuation length (in μm) for a photon in silicon, the sigma (in μm) of gaussian profile of the laser in a plane perpendicular to the direction of motion, the divergency (in $\pm$ degrees) of the beam caused by focusing lenses, the aluminium reflectivity (in %), the reflectivity (in %) of the interface between the silicon and air, the number of events to be simulated, the inner angle of laser (in degrees) and the interstrip position (in pitch) where the laser enters the detector. The detector geometry is defined in the input file containing the histograms of electric potential, electric field, etc. The result of the simulation is saved in CWN ntuple [24].

- `simulation/partntuple` - the simulation of a detector response to the particle that losses the energy according to the distribution generated in `simulation/landau` program and deposits it uniformly along the track. (The generated `hbook` file of energy loss distr. must be saved in directory `./datafiles`.) The parameter file `partprop.par` specifies the width of aluminium layer (in μm), the depth of p^+ layer (in μm),

the number of simulated events and the angle of incidence. The particles are automatically generated uniformly incident between two strips. The result is saved in CWN ntuple.

- `simulation/partgeant3` - the full simulation of a detector response to the elementary particles. As an input only the field map file is needed. The parameter file `partprop.par` specifies, except for the parameters described in previous item, the type of a particle, e.g. a pion, and its lab. momentum in GeV/c. Simultaneously, the interstrip position (in pitch) where the particle crosses the detector can be specified. (The value -1 corresponds to the uniform distribution between two strips.) The result of the simulation is saved in `hbook` format.

Still one more comment to the `simulation/bin` directory. It contains the "makefile" `g77l` necessary for compiling and linking the libraries to the source code.

To recap, let us summarize once more the input files needed for the simulation. Each simulation program reads the geometry of the detector from the field map file. The histograms of electric field and weighting field necessary for the simulation of the charge collection are saved here. Moreover, the two simulations of the response to a particle need to know the energy loss distribution. The simpler alternative (`simulation/partntuple`) reads the distribution from a file generated by the program `simulation/landau`, the full simulation program (`simulation/partgeant3`) defines the geometry in the source code and generates the energy loss itself, including the created secondary particles, e.g. δ-electrons.

In order to show how much time the program needs for the simulation of a detector response to a particle incident randomly between two strips, 10 000 events has been generated at a linux machine with a Pentium 3 processor (900 MHz) and 256 MB operational memory. The total time needed for the simulation has been ≈ 25 min.

References

[1] Ansoft Corporation: *Maxwell 2D*, student version 9.0 of electric field simulator
`http://www.ansoft.com`

[2] ATLAS Collaboration (1994): *ATLAS Technical Proposal for a General-Purpose pp Experiment at the Large Hadron Collider at CERN*, CERN/LHCC/94–93, CERN, Geneva

[3] ATLAS Inner Detector Community (1997): *ATLAS Inner Detector Technical Design Report*, Volume I, CERN/LHCC/97–16, CERN, Geneva

[4] ATLAS Inner Detector Community (1997): *ATLAS Inner Detector Technical Design Report*, Volume II, CERN/LHCC/97–17, CERN, Geneva

[5] Barr A., et al. (2001): *Beamtests of Prototype ATLAS SCT Modules at CERN H8 in June and August 2000*, ATLAS Internal Note, ATL–INDET–2002–05, CERN, Geneva

[6] Barr A. J., et al. (2001): *Beamtests of ATLAS SCT Modules in August and October 2001*, ATLAS Internal Note, ATL–INDET–2002–024, CERN, Geneva

[7] Bichsel H. (1988): *Straggling in Thin Silicon Detectors*, Reviews of Modern Physics, Vol. 60, p. 663–699

[8] Campabadal F., et al. (2005): *Beam Tests of ATLAS SCT Silicon Strip Detector Modules*, Nuclear Instruments and Methods in Physics Research A 538, p. 384–407

[9] Doležal Z., et al. (2006): *Laser Tests of Silicon Detectors*, accepted to be published by Nuclear Instruments and Methods in Physics Research A

[10] He Z. (2001): *Review of the Shockley-Ramo Theorem and Its Application in Semiconductor Gamma-ray Detectors*, Nuclear Instruments and Methods in Physics Research A 463, p. 250–267

[11] Kodyš P.: private communication

[12] Lassila-Perini K., Urbán L. (1995): *Energy Loss in Thin Layers in GEANT*, Nuclear Instruments and Methods in Physics Research A 362, p. 416–422

[13] Loparco F., Mazziotta M. N., et al. (2004): *A New Monte Carlo Code for Full Simulation of Silicon Strip Detectors* , Nuclear Instruments and Methods in Physics Research A 533, p. 322–343

[14] Lutz G. (1999): *Semiconductor Radiation Detectors*, Springer, Berlin

[15] Palik E. D. (1998): *Handbook of Optical Constants of Solids III.*, Academic Press, New York

[16] Particle Data Group (2002): *Particle Physics Booklet*, CERN, Geneva, [online]
`http://pdg.lbl.gov/`

[17] Press W. H., et al. (1992): *Numerical Recipes in Fortran: The Art of Scientific Programming*, second edition, Cambridge University Press

[18] Řezníček P. (2003): *Tests of Semiconductor Microstrip Detectors of ATLAS Detector*, diploma thesis, Prague

[19] SCT Group Prague: *SCT Prague production www page*
`http://www-ucjf.troja.mff.cuni.cz/~sct/prod`

[20] SCT Group Prague: *Simulation www page*
`http://www-ucjf.troja.mff.cuni.cz/~sct/sim`

[21] Sze S. M. (2001): *Semiconductor Devices, Physics and Technology*, second edition, John Wiley & Sons Inc., New York

[22] *User's Guide to CERNLIB – CERN Program Library Short Writeups*, CERN, Geneve, [online]
`http://wwwasd.web.cern.ch/wwwasd/cernlib`

[23] *User's Guide to GEANT – Detector Description and Simulation Tool*, CERN, Geneve, [online]
`http://wwwasd.web.cern.ch/wwwasd/geant`

[24] *User's Guide to HBOOK – Statistical Analysis and Programming*, CERN, Geneve, [online]
`http://wwwasdoc.web.cern.ch/wwwasdoc`

[25] *User's Guide to ROOT – an object-oriented data analysis framework*, CERN, Geneve, [online]
`http://root.cern.ch`

[26] Vos M. (2003): *The ATLAS Inner Tracker and the Detection of Light SuperSymmetric Higgs Boson*, phd thesis, IFIC, Valencia